Pericytes from individuals with multiple sclerosis show reduced contractility but remain responsive to myelin debris, hypoxia, and inflammatory cytokines.

Authors:

Alastair J Fortune[1], Natalie E King[1], Roisin A Moloney[1], Jake M Cashion[2], Ariane Gélinas-Marion[1], Ming Chen[1], Kathryn P Burdon[1], Jac C Charlesworth[1], Bruce V Taylor[1], Brad A Sutherland[2], Jessica L Fletcher[1*], Nicholas B Blackburn[1*], Kaylene M Young[1*#]

Affiliations:

[1] Menzies Institute for Medical Research, University of Tasmania, 17 Liverpool St, Hobart, Australia, 7000

[2] Tasmanian School of Medicine, University of Tasmania, 17 Liverpool St, Hobart, Australia, 7000

* Authors contributed equally to this work

Corresponding author (kaylene.young@utas.edu.au)

Abstract:

Multiple sclerosis (MS) is a complex inflammatory, demyelinating, and neurodegenerative disease of the central nervous system (CNS), that is accompanied by vascular abnormalities such as cerebral hypoperfusion, neurovascular uncoupling, and blood–brain-barrier (BBB) disruption. Pericytes regulate cerebral blood flow at capillaries and maintain the BBB and pericyte dysfunction may play a role in MS pathogenesis. By studying induced pluripotent stem cell-derived pericytes (iPSC-pericytes), we determined that pericytes from people with relapsing-onset MS (RoMS) have an altered transcriptome, increased cell size, and respond weakly to the vasoconstrictor, endothelin-1. This phenotype was more severe in iPSC-pericytes from a high incidence MS family, and while the individual isogenic correction of two rare genetic variants carried by this family did not modify the phenotype, our data indicate a genetic basis for pericyte dysfunction in RoMS. Intrinsic RoMS iPSC-pericyte dysfunction did not impact their capacity to respond to MS-relevant stimuli. Control and RoMS iPSC-pericytes phagocytosed myelin debris. They also proliferated, elongated, and upregulated angiogenesis signalling in response to hypoxia. Furthermore, while TNFα and IFNγ exposure caused control and RoMS iPSC-pericytes to contract more strongly in response to endothelin-1, the proportional increase was greater in RoMS iPSC-pericytes. These data suggest that intrinsic pericyte dysfunction would impair cerebral blood flow regulation prior to MS clinical onset, and their failure to regulate blood flow within MS lesions would contribute to neurodegeneration.

Keywords: pericytes, multiple sclerosis, contractility, cytokines, hypoxia, myelin, iPSC

Main

Multiple sclerosis (MS) is characterised by blood-brain-barrier (BBB) disruption (Cramer et al., 2014; Leech et al., 2007; Plumb et al., 2002; Zierfuss et al., 2024), central nervous system (CNS) inflammation, demyelinated lesions and neuron death (Woo et al., 2024). However, people with MS also experience cerebrovascular pathology, including cerebral hypoperfusion that affects the grey (de la Pena et al., 2019; Hojjat et al., 2016; Mascali et al., 2023; Stickland et al., 2019) and white matter (Adhya et al., 2006; Law et al., 2004; Varga et al., 2009). The reduction in blood flow or exchange may directly contribute to the development of hypoxia in MS brain tissue (Adingupu et al., 2023; Burtscher et al., 2025; Williams et al., 2024; Yang and Dunn, 2015), and even exacerbate the level of neuroinflammation and neurodegeneration. The underlying cause of hypoperfusion is unknown, but may implicate early changes to the vasculature or the neurovascular unit of people with MS.

The neurovascular unit is the multi-cellular complex of endothelial cells, astrocytes and pericytes that forms and maintains the BBB, and ensures that blood flow in modulated in response to the changing energy and oxygen demands of the CNS (Cashion et al., 2023; Gonzales et al., 2020; Hall et al., 2014). In people with MS, it is possible that neurovascular cells are intrinsically dysregulated (Fortune et al., 2022a), causing BBB breakdown (Plumb et al., 2002), reduced cerebral blood flow (Adhya et al., 2006; Hojjat et al., 2016) and impaired neurovascular coupling (Marshall et al., 2016; Marshall et al., 2014). Over 200 putative MS-associated susceptibility variants have been identified (International Multiple Sclerosis Genetics Consortium, 2019), and many of these are expressed by cells within the neurovascular unit (Absinta et al., 2021; International Multiple Sclerosis Genetics Consortium, 2019). These or other variants account for the intrinsic dysfunction of MS iPSC-derived endothelial cells, which are larger, promote immune cell interaction, and form weaker endothelial cell barriers (Nishihara et al., 2022). It is also possible that the neurovascular unit is compromised during immune cell infiltration or by other MS pathophysiological stimuli, such as the accumulation of myelin debris, hypoxia or inflammatory cytokines. For example, exogenous signalling to endothelial cells and astrocytes can disrupt BBB integrity and impair blood flow regulation (D'Haeseleer et al., 2013; Ponath et al., 2017; Zhou et al., 2019a).

Brain pericytes contribute to BBB maintenance and are critical, dynamic regulators of cerebral blood flow (Brown et al., 2019; Hall et al., 2014), but few studies have explored their role in MS pathogenesis or progression (Cashion et al., 2023). Pericytes can be identified by their expression of platelet-derived growth factor receptor β (PDGFRβ), the NG2 proteoglycan, CD13 and ATP13A5 (Guo et al., 2024), and while PDGFRβ^{+} cells are present within MS lesions, their phenotype and density has not been reported (Dias et al., 2021; Kaushik et al., 2021). Importantly, pericyte depletion is sufficient to reduce BBB integrity, upregulate leukocyte adhesion molecules on endothelial cells, and promote peripheral immune cell infiltration (Armulik et al., 2010; Cashion et al., 2025; Torok et al., 2021). This may be relevant to MS pathophysiology after disease onset, as pericyte density is reduced in the cerebellum of experimental autoimmune encephalomyelitis (EAE) mice (Kaushik et al., 2021).

Pericytes can also produce inflammatory cytokines, such as CCL2/MCP-1, and enhance macrophage migration through endothelial cell coated transwells (Kaushik et al., 2021). Conversely, in response to hypoxia-induced myelin damage, pericyte growth hormone receptor signalling can promote angiogenesis and myelin repair (Ren et al., 2024; Ribatti et al., 2011). It is unclear how pericyte function is impacted by a person's genetics prior to MS onset, and the combination of genetics and pathological signalling within the MS lesion environment.

Here in, we report that RoMS iPSC-pericytes exhibit an altered contractile gene expression profile, have an impaired contractile response to endothelin-1 (ET1), and have an enlarged cell morphology. These phenotypes were more pronounced in RoMS iPSC-pericytes from a multi-case MS family, and while the isogenic correction of individual rare variants identified in MS cases did not rescue these phenotypes, our results indicate that there is a genetic basis for pericyte dysfunction in MS. We also report that pericyte function is modulated by lesion-associated stimuli including hypoxia and inflammatory cytokines. Notably, pre-exposure to TNFα and IFNγ drives an excessive contractile response to ET1 that would be predicted to impede capillary blood flow. These findings position pericytes as active participants in MS pathogenesis and progression, and a potential therapeutic target.

Results

Transcriptomic analysis of RoMS iPSC-pericytes points to an altered actin cytoskeleton and impaired contraction.

To determine whether pericytes are intrinsically altered in people with MS, we obtained blood from people without MS (n=10, controls), belonging to a multi-case MS family (n=4 familial RoMS cases spanning 2 generations) or unrelated people with RoMS (n=8 sporadic RoMS cases) for iPSC generation as previously described (Fortune et al., 2022b; Mehta et al., 2021). The resulting 22 iPSC lines (**Table 1**) were differentiated into iPSC-pericytes, using a validated protocol (Faal et al., 2019; King et al., 2024) (**Fig. 1a**) and immunocytochemistry performed to confirm the expression of PDGFRβ and CD13 (ANPEP) (**Fig. 1b**) by > 95% of the cells in each culture (**Fig. 1c**). iPSC-pericytes were subsequently harvested for bulk RNA sequencing to confirm successful differentiation i.e. the resulting cells did not resemble iPSCs or CNS cell types (**Fig. S1a**), but clustered with primary human brain vascular pericytes by principal component analysis (PCA) (**Fig. 1d**). We also aimed to determine whether iPSC-pericyte structure or function could be impacted by variants in putative MS susceptibility genes. *In vivo*, pericytes express a number of putative MS susceptibility genes (Absinta et al., 2021), and we determined that 142 of the 551 MS susceptibility genes identified by the International Multiple Sclerosis Genetics Consortium (2019) were upregulated during iPSC-pericyte differentiation (**Fig. S1b, Data S1**).

To investigate whether RoMS iPSC-pericytes have an intrinsically altered gene expression profile, we compared the transcriptome of control and familial RoMS iPSC-pericytes. After controlling for 1 factor of unwanted variation calculated using RUVseq and performing PCA, we found that control and familial RoMS samples did not form distinct clusters but showed some degree of separation along PC1 (30% of variance;

Fig. 1e). Differential gene expression analysis was performed using a log fold change threshold of 0.1 and $\alpha < 0.05$ and identified 125 differentially expressed genes (DEGs) (**Fig. 1f**). DEGs included known regulators of cell contraction, including the decreased expression of *TNNC1* and *TNNT1* (**Fig. 1g, Data S2**), which encode Troponin C1 and T1, respectively. TNNC1 and TNNT1 are best known for their role in regulating skeletal muscle contraction (Amarasinghe et al., 2016; Dyer et al., 2009), but also impact actin cytoskeletal function in other cell types (Johnston et al., 2018). We also detected changes in the expression of myosin genes (*MYO5C*, *MYO15B* and *MYL9*) and Rho GTPase activators (*ARHGAP28* and *ARHGAP29*), which all interact with or modulate actin filaments (Li et al., 2024a). Accordingly, gene set enrichment analysis revealed that skeletal muscle contraction genes were supressed (**Fig. 1h, Data S3**), suggesting that the familial RoMS iPSC-pericyte cytoskeleton may be altered in a way that impairs contractility.

RoMS iPSC-pericytes are enlarged and have a reduced endothelin-1 evoked contractile response

As changes to the actin cytoskeleton could impact cell division (Provenzano and Keely, 2011), cell shape / size (Brown et al., 2023; Kutcher et al., 2007), motility or contractility, we first exposed control, familial RoMS and sporadic RoMS iPSC-pericytes to the thymidine analogue, ethynyl-2'-deoxyuridine (EdU), for 20 hours. EdU^+ pericytes were detected in each culture (**Fig. S1c**) and the rate of pericyte division was unaffected by MS status (**Fig. S1d**). Additionally, within control, familial RoMS and sporadic RoMS iPSC-pericyte cultures, individual cells adopted the characteristic standard, spindle, sheet or circular morphologies (**Fig. 5e**), that we have previously reported (Brown et al., 2023; King et al., 2024). The standard morphology was the most prevalent in all cultures, and the distribution of morphologies was not impacted by MS status (**Fig. S1e**). Consistent with this, iPSC-pericyte elongation, indicated by maximum Feret diameter (diameter at widest point / perimeter length), was unaffected by MS status (**Fig. S1f**). However, by tracing the perimeter of individual pericytes in each culture (**Fig. 2a**), and quantifying cell area and perimeter length, we determined that familial and sporadic RoMS iPSC-pericytes were larger than control iPSC-pericytes (**Fig. 2b,c**). The increased size of RoMS iPSC-pericytes did not impact general motility or the rate of adhesion after replating (**Fig. S1g-j**), but suggested a change in metabolic regulation, cytoskeletal structure or contractility state.

To explore the capacity for iPSC-pericytes to contract, they were exposed to the potent vasoconstrictor, ET1 (Faraco et al., 2013; King et al., 2024; Neuhaus et al., 2017). We visually confirmed that 50nM ET1 exposure induced iPSC-pericyte contraction by performing time-lapse imaging of control iPSC-pericytes (**Fig. S1k**). Pericyte cell size decreased within 20 minutes of ET1 exposure and returned to baseline by 60 minutes (**Fig. S1l**). We next quantified the ET1-evoked contraction in control, familial RoMS, and sporadic RoMS iPSC-pericytes using the high throughput xCELLigence real-time cell system, which measures electrical impedance (cell index), which goes down when cells contract and cover a smaller surface area of the plate. Control, familial RoMS and sporadic RoMS iPSC-pericytes reached their maximal contractions ~14 minutes

following ET1 exposure. However, ET1 evoked a larger contraction in control iPSC-pericytes than RoMS iPSCs. The maximum contraction of familial RoMS iPSC-pericytes was ~64.1% that evoked in control iPSC-pericytes, and the maximum contraction of sporadic RoMS iPSC-pericytes ~78.3% that of control iPSC-pericytes (**Fig. 2d,e**). These data suggest that RoMS iPSC pericytes are less sensitive to ET1 or the cytoskeletal response is impaired. As ET1 receptor (*EDNRA* and *EDNRB*) gene expression is unchanged, but contractility gene expression is altered in RoMS iPSC-pericytes, the latter offers the more likely explanation.

As pericytes modulate blood flow through vasoconstriction and vasodilation (Hall et al., 2014; King et al., 2024), we evaluated the capacity of RoMS iPSC-pericytes to relax when exposed to the vasodilator, adenosine (Brown et al., 2023; King et al., 2024). iPSC-pericyte cultures experienced an initial contraction due to temperature change when the e-plate is removed from the incubator, and this is followed by a relaxation due to the addition of 10μM adenosine (**Fig. 2g**). The maximum relaxation and volume of relaxation were equivalent for control and familial RoMS iPSC-pericytes (**Fig. 2h,i**). As pericytes hold capillaries in a partially constricted state at rest and dynamically relax or contract to support the increased perfusion of metabolically active regions (Gonzales et al., 2020; Hall et al., 2014), cells that respond appropriately to vasodilators but not vasoconstrictors would be unable to maintain tone at rest or actively vasoconstrict to preferentially redirect blood flow to active areas. This would increase blood volume but reduce flow rate / exchange, and result in hypoperfusion, as detected in the brains of people with clinically isolated syndrome (Papadaki et al., 2012), an early clinical presentation that can presage an MS diagnosis.

Correcting a rare variant in PARVB or *PARD3 is insufficient to rescue familial RoMS iPSC-pericyte size or contractility*

The intrinsic dysfunction of familial and sporadic RoMS iPSC-pericytes is modulated by the combination of rare and common variants in the genome of the individual. MS is a complex polygenic disease, and most MS-associated common genetic variants have a small effect on MS risk (International Multiple Sclerosis Genetics Consortium, 2019). Rare genetic variants can have a larger effect on protein and cellular function (Singh et al., 2022), and while they are more difficult to identify, the presence of multiple affected individuals in high incidence MS families, increases the likelihood of identifying such rare, disease-associated variants (Glahn et al., 2019). As contractility was most dysregulated in the iPSC-pericytes from the multi-case RoMS family, we analysed the genomes of MS-affected family members to identify rare coding variants that may associate with MS development. We performed whole genome sequencing (WGS) on MS affected and unaffected family members (**Fig. 3a**) and applied a variant filtering pipeline to identify rare variants that segregate with MS status, and that are predicted to be deleterious to protein function (**Fig. 3b**). This led to the identification of 27 rare variants (**Table S1**). A protein–protein interaction analysis identified 2 networks, linking variant-containing genes with metabolic processes (*PLOD3* and *ACACA*) or cytoskeletal regulation (*ANK3*, *ACTR8* and *PARVB*; **Fig. S2a**), consistent with findings from our iPSC-pericyte RNA-sequencing data (**Fig 1h**). A limited functional knowledge of some genes prevented their inclusion in established networks,

despite predicted or known roles in actin and adhesion pathways. This includes *PARD3* and *AVIL*, which are linked to contractility (Dessalles et al., 2021; Gharanei et al., 2020). The predicted deleterious variant in *PARVB* (rs375241184; **Fig. 3c**) was a promising candidate from the cytoskeletal network (**Fig. S2a**) for functional interrogation, as the deletion of *PARVB* enlarges endothelial cells (Javerzat et al., 2009), and the encoded protein, β-parvin, regulates cardiomyocyte contractility (Thievessen et al., 2022). The variant in *PARD3* (rs367757939; **Fig. 3c**) represented a promising candidate for functional interrogation that sat outside of the network, due to its high Combined Annotation Dependent Depletion score (CADD) > 25 score, an established role in cell polarity and microtubule dynamics (Schmoranzer et al., 2009) which impact pericyte contraction (Dessalles et al., 2021), and its high expression by pericytes in post-mortem MS tissue (Jäkel et al., 2019; Macnair et al., 2025).

All familial RoMS iPSC lines carried the *PARVB*^{D343N} and *PARD3*^{S774Y} variants. One familial RoMS iPSC line (MNZTASi002-A, generated from individual 2-1 in the pedigree) underwent genome editing with guide RNAs to direct the correction of the *PARVB*^{D343N} or *PARD3*^{S774Y} variants to the reference allele. Following PCR and Sanger sequencing confirmation, isogenic variant-corrected clones were expanded and the resulting iPSC lines (n=3 per variant) were characterised as previously described (Fortune et al., 2022b; Mehta et al., 2021). The MNZTASi002-A familial RoMS iPSC line was also exposed to a “sham editing” procedure (Cas9 protein but no guide RNA) and unedited clones (n=3) were similarly expanded and characterised (**Fig. 3d**). The resulting iPSC lines were differentiated to generate iPSC-pericytes for morphological analyses (**Fig. 3e**). Familial RoMS iPSC-pericyte area and maximum feret diameter were equivalent for unedited and variant-corrected lines (**Fig. 3f,j**). Similarly, when familial RoMS iPSC-pericytes were exposed to ET1, the evoked contraction was not altered by the correction of the rare *PARVB*^{D343N} or *PARD3*^{S774Y} variant (**Fig. 3h,i**). These data indicate that the impaired contractility of familial RoMS iPSC-pericytes cannot be solely attributed to either the *PARVB*^{D343N} or *PARD3*^{S774Y} variant and indicates that the intrinsic change in pericyte morphology and contractility is the result of other variants, or interactions between multiple common and rare variants.

iPSC-pericytes phagocytose myelin debris

Genetic risk factors that drive MS development differ from those influencing disease severity, with the latter primarily shaped by variants that impact CNS-resident cells (Jokubaitis et al., 2023). However, little is known about how pericytes respond to stimuli present within the MS lesion environment. For example, myelin debris is present within MS lesions, and can be phagocytosed and cleared by microglia and astrocytes (Ponath et al., 2017). Endothelial cells have also been shown to phagocytose myelin debris in response to spinal cord injury and EAE (Zhou et al., 2019a), suggesting that vascular cells may also take part in myelin clearance in MS. Pericytes can phagocytose aggregated amyloid β42 (Ma et al., 2018), and a descriptive electron microscopy study of C7 ventral root avulsion in cats reported myelin sheath-like structures within pericyte phagosomes (Holtzer et al., 1998). To explore the capacity of iPSC-pericytes to phagocytose myelin, they were plated onto

pHrodo-myelin coated plates and imaged for 24 hours (**Fig. 4a**). Shortly after pericyte attachment, pHrodo signal was detected within the pericytes, indicating that myelin debris was within acidic phagolysosomes (**Fig. 4b**). By 24 hours, >85% of iPSC-pericytes were pHrodo-myelin$^+$ and the rate of cell labelling was not impacted by MS status (**Fig. 4c**). As most pericytes became pHrodo-myelin$^+$, we quantified the proportion of iPSC-pericyte area with pHrodo$^+$ pixels as a proxy for myelin debris burden and found that the pHrodo-myelin$^+$ area was equivalent in control and familial RoMS iPSC-pericytes (**Fig. 4d**). After 20 hours on myelin debris, iPSC-pericytes could still proliferate, and myelin exposure did not alter their morphology or motility (**Fig. 4e-i**), suggesting that myelin phagocytosis is not toxic to pericytes. It has been reported that myelin debris clearance is impaired in pericyte-deficient mice following middle cerebral artery occlusion (Shibahara et al., 2020), and our data indicate that this could be a direct result of pericytes normally supporting myelin clearance following a demyelinating injury.

To determine whether exposure to or phagocytosis of myelin debris results in transcriptional changes in iPSC-pericytes, we performed bulk RNA sequencing of control and familial RoMS iPSC-pericyte cultures at 48 hours of myelin exposure. PCA of global gene expression indicated that cell line was the primary source of variation, and that myelin treatment did not have a significant effect on gene expression profile (**Fig. 4j**). Differential gene expression analysis confirmed that myelin phagocytosis did not change the iPSC-pericyte transcriptional profile (**Fig. 4k, Data S4**) of control or familial RoMS iPSC-pericytes (**Fig. S3a, Data S7**). These data indicate that pericytes respond differently to other cell types, including astrocytes, microglia, and brain microvascular endothelial cells, which change their proliferation rate and gene expression in response to myelin debris exposure (Baaklini et al., 2023; Ponath et al., 2017; Zhou et al., 2019a). Our data do not rule out the possibility that myelin exposure modifies protein translation or phosphorylation in pericytes, rather than gene transcription.

Hypoxia increases proliferation, morphological remodelling, and angiogenic signalling in iPSC-pericytes

Within MS lesions, pericytes would be exposed to a hypoxic environment (Adingupu et al., 2023; Halder and Milner, 2021; Williams et al., 2024; Yang and Dunn, 2015). Pericytes are early responders to brain hypoxia, with many commencing migration along vessels within 2 hours of a hypoxic injury (Gonul et al., 2002). *In vitro*, hypoxic human brain vascular pericytes rapidly upregulate hypoxic and inflammatory signalling pathways (Carlsson et al., 2018), but the functional consequences are poorly understood (Carlsson et al., 2023). To determine how hypoxia impacts iPSC-pericyte behaviour and determine whether RoMS status alters this response, we cultured control and familial RoMS iPSC-pericytes under normoxic or hypoxic (0.5% O_2) for 20 hours. Normoxic and hypoxic iPSC-pericytes incorporated EdU (**Fig. 5a**), however, the proportion of EdU$^+$ iPSC-pericytes increased significantly under hypoxic conditions (**Fig. 5b**). This response is consistent with that of immortalised retinal pericytes, which also increased their proliferation rate when cultured with <1% O_2 (Liu et al., 2025). Of note, control and familial RoMS iPSC-pericytes equally increased their proliferation in

response to hypoxia (**Fig. 5b**), indicating that this response is not altered by RoMS status.

Hypoxia can induce actin cytoskeletal remodelling and morphological change (Huang et al., 2019; Macharia et al., 2021), and was associated with a reduction in cell area for iPSC-pericytes (**Fig. 5c**). However, we detected a significant interaction between hypoxia and MS status, consistent with a larger morphological change in familial RoMS iPSC-pericytes compared with controls. Indeed, under hypoxic conditions, familial RoMS iPSC-pericytes became the same size as hypoxic control iPSC-pericytes (**Fig. 5c**). *In vitro* and *in vivo* evidence suggests that pericytes initially contract in response to hypoxia and, upon dying, remain in a constricted state (Hall et al., 2014; Islam et al., 2024; Yemisci et al., 2009). While we cannot directly attribute the reduction in control or familial RoMS iPSC-pericyte size to a contractile response, this may, at least partly, explain this phenotype. However, familial RoMS iPSC-pericytes also increased their max Feret diameter in response to hypoxia, suggesting they also became more elongated (**Fig. 5d**). This did not reflect a selective change in morphological type within the hypoxic familial RoMS iPSC cultures, as a higher proportion of control and familial RoMS iPSC-pericytes adopted the elongated spindle morphology, at the expense of sheet pericytes, under hypoxic conditions (**Fig. 5e,f**). Additionally, control and RoMS iPSC-pericytes more frequently organised themselves into chains of 3-8 pericytes (**Fig. 5g**). These cells only represented ~1-2% of the iPSC-pericyte population but produced a striking change in culture appearance between normoxic and hypoxic conditions (**Fig. 5h**). Hypoxic control and RoMS iPSC-pericytes also more motile, increasing their velocity and nuclear displacement (**Fig. S4a,b**), consistent with a previous study of retinal pericytes (Liu et al., 2025). We speculate that the pericyte chains recapitulate the end-to-end pericyte organisation along blood vessels *in vivo* (Berthiaume et al., 2018). This morphological change may also reflect an attempt to facilitate angiogenesis, as pericytes are recruited by newly generated endothelial tip cells to form a supporting scaffold structure for new vessels, and support extension of the basement membrane (Ribatti et al., 2011).

To uncover the molecular drivers of these hypoxia-induced morphological and behavioural changes and determine if MS status shapes this response, we performed bulk RNA sequencing on control and familial RoMS iPSC-pericytes cultured under normoxic and hypoxic conditions. By comparing gene expression in control and familial RoMS hypoxic iPSC-pericytes and assessing genes for an interaction between disease status and hypoxia, we identified one gene, sorting nexin 8 (*SNX8)*, that is selectively downregulated in hypoxic familial RoMS iPSC-pericytes (**Fig. S3b, Data S8**). SNX8 is a protein involved in autophagy, endosome recycling and lysosome tubulation (Li et al., 2024b) suggesting that, under hypoxic conditions, familial RoMS iPSC-pericytes may have an impaired ability to degrade and remove cellular waste. As these data demonstrated that the iPSC-pericyte transcriptional response to hypoxia was not significantly modified in people with RoMS, our further comparisons more broadly aimed to characterise the iPSC-pericyte response to hypoxia.

PCA of global gene expression revealed that pericytes clustered by hypoxic treatment along PC1 and accounted for 24% of sample variation (**Fig. 5i**). When comparing

iPSC-pericytes cultured under normoxic or hypoxic conditions, >1,900 genes were differentially expressed (log fold change threshold = 0.585), and most DEGs were upregulated with hypoxia (**Fig. 5j, Data S5**). iPSC-pericytes exposed to myelin debris and hypoxia had a transcriptomics profile equivalent to hypoxia alone, confirming that exposure to myelin debris did not alter gene transcription, even in the context of hypoxia (**Fig. S3c**). Amongst the DEGs, we identified genes that regulate the cell cycle and proliferation, including *PDGFB*, (**Fig. 5l, Fig. S4c**), and likely promote the hypoxia-induced increase in iPSC-pericyte proliferation. Gene set enrichment analysis, using gene ontology (GO) biological processes, identified 221 significantly enriched terms (*p-adjusted* < 0.05; **Data S6**). Hypoxic iPSC-pericytes suppressed the transcription of genes related to mitochondria and ribosome function, and increased the transcription of hypoxic responsive genes and genes associated with blood vessel morphogenesis (**Fig. 5k**). Key genes that were differentially expressed and relevant to the enriched terms angiogenesis, the cytoskeleton, and antigen presentation are shown in **Fig. 5l and S4g**. These included *ANGPTL4*, which encodes angiopoietin-like 4 (Hung et al., 2021; Sodhi et al., 2019), and Human Leukocyte Antigen DR Beta 1 (*HLA-DRB1*), for which specific variants are significantly associated with an increased risk of developing MS (International Multiple Sclerosis Genetics Consortium, 2019).

To determine which transcription factors could drive the hypoxic transcriptional response, we calculated transcription factor enrichment scores using decoupleR. This analysis revealed that HIF1α was activated while SREBF1 and SREBF2 were suppressed (**Fig. S4d**). The hypoxic-mediated degradation of the SREB transcription factors is known to downregulate cholesterol synthesis, which is an oxygen intensive process (Dickson et al., 2023), and likely represents a pro-survival response in hypoxic iPSC-pericytes. Further analysis of hypoxic inducible factor (HIF) signalling revealed that hypoxic iPSC-pericytes expressed lower levels of HIF genes, but increased transcription of the antisense gene, *HIF1A-AS3*, which supresses *HIF1A* and *HIF2A* expression (Downes et al., 2023) (**Fig. S4e**; for specific genes and processes under the control of *HIF1A,* see **Fig. S4f,g**). These data suggest that pericytes would be highly responsive to hypoxia and likely undergo morphological and transcriptional changes driven by hypoxia within the MS lesion environment.

Cytokines increase ET1-evoked iPSC-pericyte contractility

To determine whether pericyte function would be impacted by exposure to inflammatory cytokines found within MS lesions, we exposed iPSC-pericytes to 20ng/ml TNFα and/or 40ng/ml IFNγ. Exposure to TNFα and IFNγ, but not either cytokine alone, significantly reduced the proportion of control and familial RoMS iPSC-pericytes that proliferated and incorporated EdU over a 20-hour period (**Fig. 6a,b**). These data are not consistent with previous studies that have reported an increase in primary mouse pericyte proliferation with cytokine stimulation (Cembran et al., 2025; Tigges et al., 2013), but may be the result of different cell sources. By assessing the morphology, we found that TNFα and IFNγ treatment increased the cell area (**Fig. 6c**) and perimeter (**Fig. S5a**) of control but not familial RoMS iPSC-pericytes. Consequently, TNFα and IFNγ treated control iPSC-pericytes reached the resting

state size of familial RoMS iPSC-pericytes (**Fig 6c**). Max Feret diameter was unchanged by cytokine treatment (**Fig. S5b**). These data suggest that iPSC-pericyte proliferation is reduced and cell size increased by dual exposure to these cytokines. Familial RoMS iPSC-pericytes may fail to increase their size due to their already increased size at baseline, or more broadly reflect their intrinsic cytoskeletal dysfunction.

To determine whether exposure to inflammatory cytokines influenced pericyte contractility and would, by extension, influence vascular tone, we exposed a single iPSC-pericyte line to TNFα and IFNγ for 1 or 20 hours, and monitored their response at ET1. The contractile response of iPSC-pericytes to ET1 was enhanced by 1 hour of TNFα and IFNγ exposure but was enhanced ~2-fold after 20 hours (**Fig. S5c**). We next exposed control and familial RoMS iPSC-pericytes to TNFα or IFNγ alone or in combination for 20 hours, before measuring the ET1-evoked contraction. TNFα or IFNγ was sufficient to increase the maximum ET1-evoked contraction in control and familial RoMS iPSC-pericytes (**Fig. 6d,e**). However, exposure to both cytokines produced a more marked effect, suggesting an additive effect (**Fig. 6d,e**). While the magnitude of the contraction evoked by ET1, following TNFα or TNFα and IFNγ treatment, was smaller in the familial RoMS compared to the control iPSC-pericytes, it represented a significantly greater fold-increase relative to the diluent-treated cells (**Fig. 6f**). In addition to the increased maximum contractility, we observed a delay in the return of cytokine-stimulated control and familial RoMS iPSC-pericytes to their baseline cell size. While diluent-treated pericytes returned to baseline within ~29 minutes of ET1 treatment, pericytes exposed to TNFα or IFNγ alone took ~40 and ~34 minutes, respectively. Notably, those treated with TNFα and IFNγ required ~54 minutes to return to their baseline cell index (**Fig. 6d,e**). This is reflected by a decrease in area under the curve during the first 50 minutes of the assay for each cytokine treatment condition (**Fig. 6g**). This larger and sustained pericyte vasoconstriction would greatly restrict blood flow to active and smouldering lesions, exacerbate cellular metabolic stress, promote neurodegeneration and impede repair (Jakimovski et al., 2022; Jakimovski et al., 2024). As reactive astrocytes in MS postmortem tissue express ET1, and astrocytes exposed to inflammatory cytokines *in vitro* release ET1 (D'Haeseleer et al., 2013; Hostenbach et al., 2019), the astrocytic response would be predicted to actively promote pericyte mediated vasoconstriction and further reduce perfusion. Indeed, the net effect of increased maximal contractility and prolonged contraction would likely be the disruption of cerebral blood flow in people with MS and enhanced neurodegeneration (Jakimovski et al., 2022).

Discussion

Here in, we determined that pericytes from individuals with familial and sporadic RoMS have larger cell bodies and smaller ET1-evoked contractions. Transcriptional differences between control and familial RoMS iPSC-pericytes suggest that this result from intrinsic changes to the RoMS pericyte cytoskeleton, including changes to myosin and Rho GTPase activator expression. As the familial RoMS pericytes were more severely affected than the sporadic RoMS pericytes, the family members may have a higher burden of genetic variants, or the presence of rare but potentially high impact genetic variants that impact pericyte structure and function. Our whole-genome sequencing data identified 27 rare variants that associated with MS in this family, and were predicted to be deleterious, however, correcting the variant in *PARVB* or *PARD3* was insufficient to rescue the size or contractile response of familial RoMS iPSC-pericytes. Intrinsic pericyte dysfunction has the potential to contribute to MS onset and pathophysiology, but did not prevent the pericytes from responding to MS-relevant environmental stimuli. Control and familial RoMS iPSC-pericytes phagocytosed myelin debris and responded to hypoxia by proliferating, changing their morphology, and upregulating signalling pathways that promote angiogenesis. iPSC-pericytes also responded to inflammatory cytokines (TNFα and IFNγ) by contracting more severely in response to ET1. These findings indicate that in people with MS, pericytes have a reduced dynamic range of contraction, which would impair their capacity to regulate brain perfusion, and may even promote MS susceptibility. After disease onset, the pericytes would respond to pathological signalling within the lesion environment in a way that would promote MS progression.

Hypoperfusion and impaired neurovascular coupling may precede MS clinical onset and even contribute to disease development (Cashion et al., 2023). Individuals with clinically isolated syndrome have reduced cerebral blood flow, increased cerebral blood volume and longer mean transit times (Papadaki et al., 2012; Varga et al., 2009). This could result from the impaired ability of RoMS pericytes to contract or relax in response to vasoactive signals. While local vasodilation is typically associated with increased regional blood flow, being unable to appropriately constrict capillaries across the cerebrovascular network would impair the fine-tuned redistribution of blood required to meet neuronal demand (Berthiaume et al., 2022; Gonzales et al., 2020). This is demonstrated experimentally, by the loss of pericytes from across the capillary bed, which results in increased capillary bed blood volume and global cerebral hypoperfusion (Cashion et al., 2025; Nikolakopoulou et al., 2019). On a smaller scale, even the focal ablation of 3 nearby pericytes can stall blood flow and cause capillary regression (Berthiaume et al., 2022). Disturbances in blood flow also alter endothelial cell phenotypes, causing endothelial cells to upregulate genes involved in immune cell chemotaxis and inflammatory responses (Andueza et al., 2020). As iPSC-derived endothelial cells from people with MS express elevated levels of the leukocyte adhesion molecules, ICAM-1 and VCAM-1 (Nishihara et al., 2022), blood flow stalling due to pericyte dysfunction, would further exacerbate immune cell binding and migration across the endothelium. Consequently, the disrupted blood flow from impaired pericyte-mediated vasoconstriction and intrinsic endothelial cell alterations

may create a vascular environment that is more permissive to immune cell infiltration, directly contributing to MS development.

Once MS develops, it is likely that the intrinsic pericyte dysfunction is overshadowed or masked by maladaptive responses to MS-relevant environmental stimuli such as hypoxia and inflammatory cytokines. People with MS have typical cerebral blood volume (Papadaki et al., 2012) but decreased cerebral blood flow (Adhya et al., 2006; Hojjat et al., 2016; Law et al., 2004). Interestingly, hypervascularisation is also a feature of MS (Buch et al., 2021; Holley et al., 2010), presumably a secondary response to the reduced blood flow and resulting hypoxia (Williams et al., 2024; Yang and Dunn, 2015). This may be explained by the response of pericytes to hypoxia. Our data demonstrate that exposure to 0.5% O_2 induces pericyte proliferation and morphological change that is accompanied by the upregulation of cell cycle, cytoskeletal, and angiogenic genes. The increase in spindle shaped pericytes and the formation of interconnected chains likely reflect a shift toward a pro-angiogenic state, as pericytes play a scaffolding role for endothelial tip cells, to direct new blood vessel formation (Coelho-Santos et al., 2021; Ren et al., 2024; Ribatti et al., 2011). Despite higher vessel densities, hypoperfusion is still observed, likely due to ongoing inflammation. The inflammatory cytokines TNFα and IFNγ rapidly enhanced ET1-induced pericyte contraction in both control and familial RoMS iPSC-pericytes. This heightened contractile response could explain the capillary narrowing and reduction in blood flow observed in MS lesions, compared to non-affected brain regions (Gaitan et al., 2013; Sisco et al., 2021). Importantly, reduced cerebral blood flow in people with MS is associated with greater white matter damage, elevated serum neurofilament light chain in the plasma, and increased neuroinflammation (Jakimovski et al., 2022; Jakimovski et al., 2024; Mascali et al., 2023). However, our finding that inflammatory cytokines increase the size and duration of pericyte contraction also has implications for other neuroinflammatory conditions, including stroke, where it likely contributes to the no-reflow phenomenon (Mujanovic et al., 2024; Yemisci et al., 2009). The potential benefit of developing and trialling therapies to restore blood flow in neurodegenerative conditions is highlighted by outcomes in EAE and Alzheimer's disease (APP^{NL-G-F}) mice that were treated with the CNS-selective vasodilator nimodipine. Blood perfusion was improved, and this was accompanied by a decrease in demyelination (EAE only), hypoxia, immune cell stalling and neurological deficits (Desai et al., 2020; Korte et al., 2024).

Our data suggest that intrinsic pericyte dysfunction may disrupt cerebral blood flow and promote MS onset and, following disease onset, respond to inflammatory and hypoxic stimuli in a way that further restricts blood flow and contributes to neurodegeneration. These findings underscore the importance of targeting pericyte function and cerebral perfusion as a therapeutic strategy in MS.

Methods

Resource availability

Further information and requests for data or resources related to this preprint should be directed to the corresponding author.

MS family whole genome sequencing

The recruitment of affected and unaffected members from high incidence MS families and the related genetic analyses were approved by the University of Tasmania Human Research Ethics Committee (26235). All study participants provided informed consent. MS cases were diagnosed by an MS neurologist, and relatives were only classified as unaffected if they were over the age of 50 years at recruitment and self-reported no clinical history of MS.

Genomic DNA was extracted from whole blood using the Qiagen QIAamp DNA blood mini kit. Illumina DNA PCR-free tagmentation library preparations were completed for each sample and 150 base pair paired end sequencing conducted at the Australian Genome Research Facility on an Illumina NovaSeq 6000 to an average of 30-fold depth genome wide with ~ 100 Gb of data generated per individual sequenced.

Genome alignment and rare variant filtering pipeline

Sarek (v3.1.2) implemented in Nextflow (v23.10.1), was used to process fastq data, align reads to the GRCh38 human reference, and conduct variant calling using GATK's haplotypecaller (Auwera and O'Connor, 2020; Poplin et al., 2018), generating per sample genome variant call format (VCF) files, followed by joint calling across the entire family to combine gVCFs into a single multi-sample VCF. On average, genome coverage depth, measured using mosdepth (v0.3.3) (Pedersen and Quinlan, 2018), was 40.4X, ranging from 28.6X to 68.9X. Somalier (v0.2.19) (Pedersen et al., 2020) was used to confirm reported pedigree relationships, and self-reported European ancestry. Multiallelic variants were split and variants left normalised with bcftools (v1.15.1). Variants were assigned a per sample quality score using GATK's VariantFiltration function, assigning a High Confidence filter to variants with depth (DP) ≥10 and genotype quality (GQ) ≥20. Variants were annotated using Ensembl's variant effect predictor (VEP; v112) (McLaren et al., 2016), and ANNOVAR (Wang et al., 2010) to provide gnomAD 4.1 allele frequency information (Karczewski et al., 2020). Variants not annotated with a CADD v1.7 (Schubach et al., 2024) score by VEP were manually scored using the CADD web server. A subset of variants were not scored using the web server, as the allele length was incompatible with the server. These variants were manually assessed in the gnomAD v4.1 database where necessary during variant prioritisation. To identify variants occurring exclusively in MS affected family members, we excluded High Confidence homozygous reference variants in affected family members. We then focussed on High Confidence variants occurring (heterozygous or homozygous) in all affected family members. These variants were subsequently filtered to identify variants with CADD Phred scaled scores ≥ 20, and gnomAD non-Finnish European (NFE) genomes minor allele frequencies of < 0.01. Finally, based on Sequency Ontology classifications we selected variants annotated

to have a MODERATE or HIGH impact consequence by VEP. Variants and their corresponding genes were subsequently reviewed and prioritised for functional work based on their known biology.

iPSC line generation and availability

All iPSC lines used in this study, including the isogenic iPSC lines, can be obtained from the MS Stem biobank (https://msresearchflagship.org.au/researchers/ms-stem). n=10 control (King et al., 2024), n=4 familial (Fortune et al., 2022b) and n=8 sporadic RoMS iPSC lines (**Table 1**) were purchased from the MS Stem biobank, Menzies Institute for Medical Research). The iPSC lines were generated and characterised as previously described (Fortune et al., 2022b; Mehta et al., 2021). The generation and use of each iPSC line was approved by the University of Tasmania Human Research Ethics Committee (approvals 16915 and 30092). All study participants provided informed consent for the blood sample collection, iPSC generation / differentiation, and genetic data sharing conducted as part of this project.

The MNZTASi002-A iPSC line underwent genome editing at the Monash Genome Modification Platform (MGMP), Monash University, to correct the PARD3^{Y774S} or PARVB^{N343D} variants to the reference allele (**Fig. 3d**). Briefly, the University of California Santa Cruz genome browser was used to identify guide RNA target sites. iPSCs were incubated with sgRNA (5ng/µl; Integrated DNA Technologies), Cas9 protein (25ng/µl), pCas9-2A-GFB plasmid (10ng/µl) and a homology directed repair oligonucleotide (6ng/µl) in OPTI-MEM for 10 minutes at ~21ºC. The medium was then replaced with mTeSR1™ Plus medium and the cells cultured for 2 days before the FACS purification and clonal culturing of GFP^{+} cells. Following PCR confirmation that variant had been corrected, Sanger sequencing was used to confirm that the variant had been corrected without introducing off-target editing near the target site. n=3 unedited (underwent genome editing without sgRNA); n=3 isogenic PARD3^{Y774S} corrected and n=3 PARVB^{N343D} corrected isogenic lines were expanded, characterised as previously described (Fortune et al., 2022b; Mehta et al., 2021) and cryopreserved in the MS Stem biobank.

iPSC culture and iPSC-pericyte differentiation

iPSCs were cultured on Matrigel® (Corning) coated 60mm Nunclon Delta plates (ThermoFisher) in mTeSR1™ Plus medium (StemCell Technologies, cat.#100-0276). iPSCs were passaged every 6-8 days and the medium exchanged every 2 days. One day prior to passaging, areas of spontaneous differentiation were removed by scraping the plate with a 200µl pipette tip and washing with DMEM/F12 (ThermoFisher). For passaging, cells were dissociated into clumps by incubating cells in ReLeSR™ (StemCell Technologies, cat.#100-0484). iPSC-pericytes were generated as previously described (King et al., 2024), by plating iPSCs in 60mm matrigel-coated plates. After 2 days, the medium was exchanged for STEMdiff™ Mesoderm Induction Medium (MIM; StemCell Technologies, #05221), replaced daily for 5 days, and Complete Pericyte Medium (CPM) containing Pericyte Growth Supplement and Fetal Bovine Serum (FBS; ScienCell, #1201), replaced daily for the subsequent 5 days. On day 10, the cells were dissociated with Accutase® (StemCell Technologies, #07922)

and plated in uncoated 6-well plates at a density of 5 x 10^4 per cm^2. The medium was replaced every 48h, and the cells passaged at ~80% confluency (~5-7 days). Passage 3-7 iPSC-pericytes were used for experiments.

Immunocytochemistry

Pericytes were grown to ~25% confluency in 24 well plates and fixed by immersion in ice-cold methanol (100%) for 10 minutes on ice (Alarcon-Martinez et al., 2018). Cells were washed with PBS and then incubated in blocking solution (10% Tween-20 / 2% FBS in PBS) for 30 minutes at 21°C. Primary antibodies (goat anti-PDGFRβ , R&D Systems AF385, RRID:AB_777165; rabbit anti-CD13, Abcam Ab108310, RRID:AB_10866195;) were diluted in the blocking solution and applied overnight at 4°C, and the plates placed on an orbital shaker. Cells were washed thrice in PBS before secondary antibodies (Alexa Fluor 488-conjugated donkey anti-rabbit; Alexa Fluor 647-conjugated donkey anti-goat) and Hoechst 33342, diluted in blocking solution, were applied for 2 hours at 21°C. Cells were washed thrice in PBS and maintained in PBS for imaging. Images were captured using an upright Nikon Eclipse Ti2 Live Cell Microscope with a 20x objective.

RNA sequencing

iPSCs were seeded on 60mm plates and cultured to ~75% confluency prior to collection. Pericytes were seeded on 6-well plates (300,000 cells per well) and cultured for 44 hours prior to collection. For hypoxia and cytokine treated pericytes, exposure to the condition was for 20 hours. For myelin treatment, cells were exposed for 44 hours. Cells were dissociated using Accutase, washed in cold DPBS and lysed using RLT buffer (Qiagen). The lysate was stored at -20°C and thawed on ice for RNA extraction using the RNeasy Mini Kit, following the manufacturer's instructions (Qiagen, #74106). Briefly, samples were transferred to RNeasy spin columns, DNA removed by treatment with DNase (Qiagen, #79254) and RNA eluted in 40µl of RNase free water. RNA concentration and integrity were evaluated using the Agilent 4200 Tapestation system. Briefly, 5µl of RNA ScreenTape Sample Buffer (Agilent, #5067-5577) and 1µl of RNA sample or ladder were combined by vortexing at 2,000rpm for 1 minute using an IKA vortex. Samples were incubated at 72°C for 3 minutes, placed on ice for 2 minutes, loaded into the TapeStation and run on RNA ScreenTape (Agilent, #5067-5576) via electrophoresis. Samples with > 20ng/µl RNA and a RNA integrity number (RIN) > 8 were sent to the Australian Genome Research Facility for bulk RNA sequencing to a minimum depth of 20 or 50 million reads with 150 base paired end lengths. Libraries were generated with the Illumina Stranded mRNA workflow with polyA capture. Raw RNA sequencing data are available upon reasonable request.

Re-analysis of publicly available RNAseq datasets

HBVP and iPSC-pericyte raw bulk RNA sequencing data from King et al. (2024) were downloaded from GEO (accession GSE252046) and the European Genome Phenome Archive (accession EGAD50000000255), respectively. Neuron, astrocyte,

oligodendrocyte, microglia and endothelial cell raw bulk RNA sequencing data from (Zhang et al., 2014) were downloaded from GEO (accession GSE52564).

RNA data processing

Raw sequencing data were processed using nf-core/rnaseq v3.12.0 (Patel et al., 2023), and a nf-core workflow executed with Nextflow v.23.04.2. Initially, the sequencing adapter (5'-CTGTCTCTTATACACATCT - 3') was trimmed from each read and 1 base pair removed from the 5' end of each read using TrimGalore (Krueger et al., 2023). A read quality Phred score threshold of 20 was used to remove low quality reads. Reads < 250 base pairs after trimming were discarded. The quality of the sequencing data was evaluated using FastQC (v.0.11.9), and all data met the necessary quality metrics for analysis. Gene expression was quantified using Salmon in mapping-based mode (v.1.10.1) with the *Homo sapiens* (Hg38) reference transcriptome. The sequencing library type was inward stranded reverse (ISR). Within Salmon, --seqBias and --gcBias were employed to enable Salmon to learn and correct for sequence-specific biases and fragment-level GC biases, respectively. The result of this analysis was per sample quantification of transcript expression.

Differential gene expression analysis and gene set enrichment

Differential gene expression analysis was performed using DESeq2 (Love et al., 2014) (v1.42.0). Tximport (Soneson et al., 2015) (v.1.30.0) was used to import transcript-level abundance into R (v.4.4.2) and summarise transcript abundance to the gene-level. Genes with < 10 reads across each group were filtered out. A first pass differential gene expression was performed comparing gene expression levels between groups. Factors of unwanted variation were estimated and removed using RUVSeq (Risso et al., 2014) (v1.36.0) as required. A *p*-value between 0.5 and 0.9 was used to define a set of genes not differentially expressed in the first pass analysis for use as in-silico empirical negative control genes in RUVSeq. Differential gene expression was tested under a hypothesis of $\log_2$ fold changes > 0.1 for control vs familial RoMS testing and 0.585 (corresponding to a 1.5-fold change in expression) for treatment testing, with a false discovery rate threshold of alpha < 0.05. Each differential gene expression analysis was visualised using EnhancedVolcano (Blighe et al., 2018) (v.1.20.0) and pheatmap (Kolde, 2012) (v.1.012). Gene set enrichment analysis (GSEA) was completed using Metascape (Zhou et al., 2019b) and clusterProfiler (Wu et al., 2021). Transcription factor analyses were completed using decoupleR (Badia-i-Mompel et al., 2022) (v.2.8.0).

EdU proliferation assay

EdU assays were performed as previously described (King et al., 2024; King et al., 2022), between passage 4 and 5. Briefly, pericytes were plated into 96-well plates at 5,000 cells per well and left to adhere overnight. The following day, the medium was replaced with CPM containing 1μM EdU (ThermoFisher) and the cells incubated for 20 hours. The medium was then removed and the cells fixed with 4% paraformaldehyde in PBS for 15 minutes at 21°C and washed with PBS. EdU incorporation was detected using the Click iT EdU proliferation kit (ThermoFisher,

#C10340) according to the manufacturer's instructions, and nuclei identified by incubation with Hoechst 33342 (ThermoFisher; #C10340; 1:1000) for 15 minutes at 21°C. Images were captured using an upright Nikon Eclipse TI Live Cell Microscope with a 10x objective. Hoechst 33342^+ nuclei were identified in each image and scored as EdU^+ when EdU fluorescence was also in the nucleus. The proportion (%) of iPSC-pericytes that had incorporated EdU was calculated as (EdU^+ Hoechst 33342^+ nuclei / total Hoechst 33342^+ nuclei) x 100. EdU assays were performed on iPSC-pericytes cultured in a standard incubator, on myelin-coated plates, under hypoxic conditions (0.5% O_2), or on myelin coated plates and in hypoxic conditions.

Motility assay

5,000 pericytes were plated per well in 96-well plates coated with poly-L-lysine ± pHrodo conjugated myelin (3µg/cm^2). Pericytes were incubated for 24 hours before being transferred to a Nikon Eclipse Ti2 Live Cell Microscope in a cage incubator (Okolab) maintained at 5% CO_2 and 37°C. To assess motility under hypoxic conditions, pericytes were placed in the cage incubator maintained at 1% O_2, 5% CO_2 and 37°C for 24 hours prior to imaging. DIC images were collected every 3 minutes for 1 hour using a 20x objective and EMCCD camera (Photometrics Evolve 512 × 512). Individual cell nuclei were annotated in each frame using QuPath (v.5.1) (Bankhead et al., 2017). Cell velocity was calculated as the change in XY coordinates of the cell nucleus between frames for each individual cell, divided by the change in time (µm/min). Nucleus displacement was calculated as the change in XY of the nucleus coordinates between the first and last frames (1 hour).

Morphology assay

Pericytes were plated into 96-well plates at 5,000 cells per well and cultured for 2 days prior to fixation with 4% paraformaldehyde in PBS for 15 minutes at 21°C, and washing with PBS. Brightfield images were taken using a Nikon Eclipse Ti2 Live Cell Microscope with a 20x objective and EMCCD camera (Photometrics Evolve 512 × 512). The outer edge of each pericyte was traced using Qupath (v.5.1) using the annotation tool. Each pericyte was manually classified using the morphological subtypes described by Brown et al. (2023). Cell area, cell perimeter and max diameter were extracted from each pericyte tracing using the Calculate Features tool. Morphological assessments were performed on iPSC-pericytes cultured in a standard incubator, on myelin-coated plates, under hypoxic conditions (0.5% O_2), or exposed to TNFα (20ng/ml) and/or IFNγ (40ng/ml).

For pericyte chain analysis, pericytes were stained with Hoechst 33342 prior to imaging using a Nikon Eclipse Ti2 Live Cell Microscope with a 20x objective and EMCCD camera (Photometrics Evolve 512 × 512). Pericytes were determined to be in a chain arrangement if 3 or more cells lined up end to end and were physically touching.

Attachment assay

Pericytes were plated into 96-well plates at 5,000 cells per well and immediately transferred to a Nikon Eclipse Ti2 Live Cell Microscope in a cage incubator (Okolab)

maintained at 5% CO_2 and 37°C. Brightfield images were collected every 10 minutes for 2 hours, and then every hour for 3 hours, using a 20x objective and EMCCD camera (Photometrics Evolve 512 × 512). The proportion (%) of pericytes, identified by DIC imaging, that had attached to the plate was quantified in each video frame.

Contractility and relaxation assays

An xCELLigence Real-Time cell analysis electrical impedance assay was used to quantify pericyte contractility or relaxation, as previously published (King et al., 2024; Neuhaus et al., 2017). Briefly, 10,000 pericytes were plated in each well of an E-plate (ACEA Biosciences, cat.#0546983000) with 150µl of CPM, and left to adhere overnight. For contractility, 50nM of endothelin-1 was added to 10µl of CPM, for each well to be assessed. The E-plate was quickly removed from the incubator, 10µl of CPM alone (diluent) or diluted endothelin-1 (50µM) added to each well, and then placed in the xCELLigence system, maintained at 37°C and 5% CO_2. For relaxation, 10µl of CPM alone (diluent) or adenosine (10µM) was used, but the E-plate was removed from incubator for 2 minutes prior adding CPM or adenosine to induce a contraction in response to the change in environmental conditions. The E-plate was then placed in the xCELLigence system. Electrical impedance, expressed as cell index, was measured every minute for 2 hours. Normalised cell index was calculated by normalising the raw cell index to the cell index value at the first timepoint. For cytokine contractility experiments, pericytes were plated into e-plates and allowed to attach for 3 hours prior to exchanging medium with cytokine containing medium. For control and familial RoMS comparisons, pericytes were incubated in cytokines for 20 hours prior to contractility assessment.

For live imaging contractility assessment, pericytes from one control cell line was plated into 96-well plates at 5,000 cells per well and cultured for 24 hours. Cells were then transferred to a Nikon Eclipse Ti2 Live Cell Microscope in a cage incubator (Okolab) maintained at 5% CO_2 and 37°C. Pericytes were incubated for 1 hour to ensure stability of pericyte contractile state, minimising the effects of moving the pericytes from the culture incubator to the microscope incubator. While the cells were maintained in the incubator, 10µl of CPM alone (diluent) or diluted endothelin-1 was added to each well. Cells were imaged every minute for an hour and frames 1, 20 and 60 used for morphological analysis. The outer edge of each pericyte was traced using Qupath (v.5.1) using the annotation tool to measure cell area at each timepoint. To assess changes in contractility, cell area measurements at frames 20 and 60 were normalised to each cell's area at frame 1 and expressed as a percentage.

Myelin extraction and pHrodo-bead conjugation

Animal experiments were approved by the University of Tasmania Institutional Biosafety Committee and Animal Ethics Committee (A0028218 and A0028287) and were carried out in accordance with the Australian Code of Practice for the Care and Use of Animals for Scientific Purposes (8th edition). Mice were housed in Optimice® microisolator cages (2-5 per cage, Animal Care Systems, Colorado, USA) maintained at 21 ± 2ºC and followed a 12-hour light/dark cycle. Mice had access to standard rodent chow (Barrastoc rat and mouse pellets) and water *ad libitum*.

Crude mouse myelin extraction was performed as previously described (Rolfe et al., 2017). Briefly, n=2 ~1 year old C57BL/6 mice (1 male and 1 female) were euthanised by CO_2 asphyxiation and the brains dissected into a sterile 6cm cell culture dish containing 0.32M sucrose 1M Tris Cl. Brain tissue was chopped into ~0.5mm^3 pieces and transferred to a sterile hand-held rotary homogeniser containing ~10mL of 0.32M sucrose 1M Tris Cl. Brain tissue was homogenised and diluted into 0.32M sucrose 1M Tris Cl. The tissue homogenate was then placed on top of 0.83M sucrose 1M Tris Cl solution in polypropylene ultracentrifuge tubes (Beckman Coutler, cat.#331372).The tissue was centrifuged at 100,000g for 45 minutes at 4°C, so that the myelin debris accumulated at the interface of the two sucrose concentrations. Myelin debris was collected, placed in new ultracentrifuge tubes and centrifuged again. The resulting myelin pellet was washed by resuspension in 1M Tris Cl buffer, centrifugation, resuspension in sterile PBS, centrifugation before being resuspended again in PBS and stored at -80°C.

Myelin was ultrasonicated using a Bioruptor® Plus sonication device (20x, 20 seconds on, 20 seconds off) in 1.5 ml Bioruptor® Plus TPX microtubes (Diagenode, cat.#C30010010-300). The myelin was then resuspended in 0.1M sodium bicarbonate buffer (pH = 8.4), prior to adding 10mM of pHrodo iFL Red STP ester, amine reactive dye (ThermoFisher Scientific, cat.#P36011) in DMSO at a concentration of 0.1µl per µg of myelin for 1 hour at RT in the dark. Labelled myelin was centrifuged at 22,000g for 5 minutes at 4°C and resuspended in sterile PBS to wash away excess dye. Finally, the labelled myelin was centrifuged at 22,000g for 5 minutes at 4°C, resuspended in sterile PBS at a concentration of 2µg per µL, and sonicated (10x, 20 seconds on, 20 seconds off), before storage at -20°C for use in experiments.

Myelin phagocytosis assay

96-well plates were incubated with poly-L-lysine (0.001%, Merck, cat.#P4707) ± pHrodo-myelin (3µg/cm^2) for 2 days before plates were washed with DPBS and the pericytes seeded at 5,000 cells per well. Seeded plates were placed in a cage incubator (Okolab) maintained at 5% CO_2 and 37°C. DIC and fluorescent images (568nm laser to detect pHrodo) were collected on a Nikon Eclipse Ti2 Live Cell Microscope using a 20x objective and EMCCD camera (Photometrics Evolve 512 × 512), every 20 minutes for 24 hours. The proportion (%) of pericytes, identified by DIC imaging, that had pHrodo$^+$ puncta, indicative of myelin phagocytosis, was quantified in each video frame. From images collected at the 24-hour timepoint, the outer edge of individual pericytes was traced using Qupath (v.5.1), and the area containing pHrodo labelling was calculated and expressed as a percentage of the total cell area.

Inducing hypoxia

To model hypoxic conditions, iPSC-pericytes were incubated in a hypoxia chamber (StemCell Technologies, #27310) with a portable oxygen monitor. A 100mm petri dish containing 5ml of dH_2O was placed in the bottom of the chamber to maintain humidity. The chamber was flushed with 5% CO_2 in N_2 until the oxygen level stabilised at 0.5%.

Cells under normoxic conditions were place in an identical but unsealed chamber. The chambers were maintained inside an incubator at 37ºC for 20 hours.

Cytokine exposure

To model inflammatory MS lesion-like conditions, iPSC-pericytes were incubated in cytokine containing media. iPSC-pericytes were cultured in TNFα (20ng/ml; StemCell Technologies, #78157.1) and/or IFNγ (40ng/ml; StemCell Technologies, #78141.1) containing CPM for 20 hours unless specified.

Statistical analyses

All quantification was performed blind to treatment condition and/or MS status. Statistical analyses were performed in R (v.4.4.2). All data unless otherwise stated were analysed by restricted maximum likelihood (REML) models with cell line as a random effect (lme4 package v.1.1-35.1). Multiple comparison post hoc (Tukey method) tests were performed utilising the Kenward-Roger method for degrees of freedom (emmeans R v.1.8.9). Proportional data was instead performed using a binomial generalised linear mixed model. Statistical significance was set as $p < 0.05$ and data are presented as group means ± SEM for column and line graphs, and median ± interquartile range for boxplots.

Acknowledgements:

This research was supported by grants from the Medical Research Future Fund (EPCD0008), the National Health and Medical Research Council (NHMRC; 2030057; 2035302; APP1163384), MS Australia (118273, 20-137, 23-0202) and the Irene Phelps Charitable Trust. A.J.F was supported by an Australian Research Training Program scholarship and a Menzies Institute for Medical Research Philanthropic Fellowship. K.M.Y was supported by a Senior Research Fellowship from MS Australia (21-3-023). J.L.F and N.B.B were supported by Research Fellowships from MS Australia (23-PDF-0121, 22-4-097). B.V.T was supported by an NHMRC Investigator Award (GNT3008389). J.M.C and M.C. were supported by Tasmanian Graduate Research scholarships. J.C.C was supported by a Henry Baldwin Senior Research Fellowship from the Menzies Institute of Medical Research.

Author Contributions:

A.J.F: methodology; validation; investigation; formal analysis; visualisation; writing – original draft; writing – review and editing. N.E.K: methodology; validation; investigation; writing – review and editing. R.A.M: investigation; formal analysis; writing – review and editing. J.M.C: methodology; investigation; writing – review and editing. A.G: investigation. M.C: formal analysis. K.P.B: methodology; supervision. J.C.C: funding acquisition; methodology; supervision. B.V.T: conceptualisation; funding acquisition. B.A.S: funding acquisition; methodology; writing – review and editing. J.L.F: conceptualisation; investigation; funding acquisition; methodology; supervision; writing – review and editing. N.B.B: conceptualisation; funding acquisition; methodology; formal analysis; visualisation; supervision; writing – review and editing.

K.M.Y: conceptualisation; funding acquisition; methodology; visualisation; supervision; writing – original draft; writing – review and editing.

Declaration of Interests:

The authors declare no competing interests.

Figure Legends

Figure 1: Gene expression differs between iPSC-pericytes from people with or without RoMS (a) Experimental design and timeline of pericyte differentiation. (b) Images (20x) of PDGFRβ (blue) and CD13 (red) expression by iPSC-pericytes. Scale bars, 50µm. (c) Quantification of the proportion of cells within iPSC-pericyte cultures that are $CD13^+$ or $PDGFR\beta^+$. Data is expressed as mean ± SEM and was analysed using a binomial generalised linear mixed model. 1 well stained per cell line for n=5 control, n=4 familial RoMS and 8 = sporadic RoMS cell lines (>100 cells evaluated per line). (d) Principal component analysis comparing gene expression for primary cells from the adult mouse brain cortex (Zhang et al. 2014), primary human brain vascular pericytes (King et al. 2024) and iPSC-derived pericytes. (e) Principal component analysis of gene expression incorporating 1 factor of unwanted variation (n=5 control and n=4 familial RoMS cell lines). (f) Volcano plot showing genes that are differentially expressed between control (n=5 lines) and familial RoMS (n=4 lines) iPSC-pericytes. Adjusted p-value < 0.05 and Log2 fold change ≥ 0.1. (g) Boxplots showing gene expression in control and familial RoMS iPSC-pericytes, for DEGs predicted to impact pericyte contractility. Data expressed as median ± interquartile range. Individual dot points represent the mean of the n=5 control or n=4 familial RoMS iPSC-pericyte cultures. (h) The top 6 activated and suppressed GO biological process ontology terms identified by gene set enrichment analysis of DEGs between control and familial RoMS iPSC-pericytes (n=5 control and n=4 familial RoMS lines). False discovery rate adjustment was used for multiple testing for RNAseq data.

Figure 2: Enlarged RoMS iPSC-pericytes have a reduced contractile response to endothelin-1. (a) Images of control, familial RoMS and sporadic RoMS pericytes with their perimeter traced for morphological assessment (red). Scale bars, 10µm. (b) Cumulative distribution plot of iPSC-pericyte cell body area. > 50 cells evaluated per cell line for n=10 control, n=4 familial RoMS and n=8 sporadic RoMS lines. Inset graph depicts the mean cell area per line ± standard deviation, and dots represent the mean for individual cell lines. (c) Cumulative distribution plot of iPSC-pericyte perimeter. > 50 cells evaluated in each of n=10 control, n=4 familial RoMS and n=8 sporadic RoMS lines. Inset graph depicts the mean cell perimeter per line ± standard deviation. (d) Normalised xCELLigence contractility cell index for control, familial RoMS and sporadic RoMS iPSC-pericytes responding to endothelin-1 over a 2 h period. 2-4 wells evaluated per cell line to obtain the average per cell line. Data presented represent the group mean ± SEM for n=9 control, n=4 familial RoMS and n=8 sporadic RoMS cell lines. (e,f) Quantification of the minimum cell index (maximum pericyte contraction) or area under the curve for the first 20 minutes following ET1 treatment of control, familial RoMS and sporadic RoMS iPSC-pericytes. 2-4 wells were evaluated to obtain the average for each cell line and data are presented as mean for each group ± SEM from n=9 control, n=4 familial RoMS and n=8 sporadic RoMS lines. (g) Normalised xCELLigence assay cell index for control and familial RoMS iPSC-pericytes following adenosine exposure. 2-4 wells were evaluated to obtain a per cell line average. Data are presented as mean per group ± SEM for n=5 control or n=3 familial RoMS lines. (h) Quantification of the maximum cell index (level of relaxation) for control and familial RoMS iPSC-pericytes exposed to diluent or adenosine. 2-4 wells were evaluated to

obtain a per cell line average. Data presented represent the mean per treatment ± SEM for n=5 control and n=3 familial RoMS lines. (i) Area under the curve for the first 20 minutes following adenosine treatment of control or familial RoMS iPSC-pericytes. # < 0.1, ∗p < 0.05, ∗∗∗p < 0.001, ∗∗∗∗p < 0.0001. Restricted maximum likelihood linear mixed model with pairwise comparisons using Tukey's adjustment for p-values.

Figure 3: Correction of a rare variant in *PARVB* or *PARD3* does not restore the ET1 contractile response of familial RoMS iPSC-pericytes. (a) Pedigree of the high incidence MS family, identifying individuals by MS status (black, MS) and whether they were whole genome sequenced (WGS, red arrows). (b) Rare variant filtering pipeline with the number of variants that surpassed each filtering step. (c) Details of the 2 prioritised rare missense variants identified in the high incidence MS family, including the amino acid change, allele frequency in non-Finnish Europeans (gnomAD v4.1) and combined annotation dependent depletion (CADD v.17) score. (d) Details of the isogenic iPSC lines in which the *PARVB*^{D346N} or *PARD3*^{S774Y} variant was corrected and the "unedited" sham CRISPR-Cas9 editing procedure was performed without guide RNAs. (e) Images of unedited, PARVB^{N346D} and PARD3^{Y774S} iPSC-pericytes traced for morphological assessment (red line denotes the cell perimeter). Scale bars, 10µm. (f) Cumulative distribution plot for iPSC-pericyte area. Data from > 50 cells per cell line and n=3 unedited, PARVB^{N346D} and PARD3^{Y774S} lines. Inset graph shows mean per group ± standard deviation, where dots represent mean area for iPSC-pericytes in individual cell lines. (g) Cumulative distribution plot for max feret diameter for iPSC-pericytes. Data from > 50 cells per line; n=3 unedited, PARVB^{N346D} and PARD3^{Y774S} lines. Inset graph shows mean max ferret diameter per group ± standard deviation, and dots represent cell line means. (h) Cell index of unedited, PARVB^{N346D} and PARD3^{Y774S} iPSC-pericytes treated with ET-1, normalised to cell index at the time of endothelin-1 addition. 2-4 wells were evaluated for a cell line average; data represent the mean per group ± SEM for n=3 unedited, PARVB^{N346D} or PARD3^{Y774S} cell lines. (i) Quantification of the minimum xCELLigence assay cell index (maximum contraction) per group for iPSC-pericytes responding to ET-1. 2-4 wells were evaluated for a per cell line average; data represent the mean per group ± SEM for n=3 unedited, PARVB^{N346D} and PARD3^{Y774S} cell lines. Restricted maximum likelihood linear mixed model with pairwise comparisons using Tukey's adjustment for p-values. WGS – whole genome sequencing, CADD – combined annotation dependent depletion, gnomAD NFE – genome aggregation database non-Finnish Europeans.

Figure 4: iPSC-derived pericytes phagocytose myelin debris but this is not associated with morphologically or transcriptional changes. (a) Schematic of mouse myelin extraction and the treatment of iPSC-derived pericytes. (b) Epifluorescence and DIC images (20x) of iPSC-pericytes cultured without (no myelin) or with pHrodo-tagged myelin debris for 20 hours. Scale bars, 50µm. (c) Quantification of the proportion (%) of control or familial RoMS iPSC-pericytes that phagocytosed myelin and became pHrodo^{+} over time (imaged every 20 minutes for 20 hours). > 50 cells evaluated per cell line; n=5 control and n=4 familial RoMS cell lines. Data expressed as mean per group ± SEM. (d) Quantification of iPSC-pericytes area with myelin-pHrodo^{+} pixels (%) was calculated for n=5 control and n=4 familial RoMS lines

(> 100 cells evaluated per line). Data expressed as median ± interquartile range, dots represent cell line mean. (e) Images (10x) of iPSC-pericytes that incorporated EdU (red) under no myelin or myelin conditions. Scale bars, 50µm. (f) The proportion (%) of iPSC-pericytes per culture that became EdU+ over 20 hours in no myelin and myelin conditions. 4-9 wells were evaluated per n=5 control and n=3 familial RoMS lines. Data are expressed as mean ± SEM, where individual dots represent the mean for each cell line. (g) Quantification of iPSC-pericyte cell area. > 50 cells were measured per line per treatment condition for n=5 control and n=4 familial RoMS lines. Data are expressed as median ± interquartile range, and individual dots represent the cell line means. (h) Quantification of the mean velocity of iPSC-pericytes under no myelin and myelin conditions. Note that velocity was determined for > 10 cells per line per treatment, and data from n=4 control and n=4 familial RoMS lines is combined and expressed as n=8, as MS status had no significant effect. Data are expressed as median ± interquartile range, and individual dots represent cell line means. (i) Quantification of nucleus displacement between t = 0 and t = 60 minutes of imaging for iPSC-pericytes under no myelin or myelin conditions. Displacement was measured for > 10 cells per line per treatment for n=8 (n=4 control and n=4 familial RoMS) lines. Data are expressed as median ± interquartile range, and individual dot points represent cell line means. (j) Principal component analysis of gene expression in no myelin or myelin treated iPSC-pericytes. (k) Volcano plot comparing gene expression in iPSC-pericytes cultured without or with myelin debris. Adjusted p-value < 0.05 and Log2 fold change ≥ 0.585; n=9 (n=5 control and n=4 familial RoMS) lines. Restricted maximum likelihood linear mixed model with pairwise comparisons using Tukey's adjustment for p-values. False discovery rate adjustment was used for multiple testing for RNAseq data.

Figure 5: Hypoxia incudes proliferation and alters the morphology and transcriptomic profile of iPSC-pericytes. (a) Images (10x) of control iPSC-pericytes that incorporate EdU (red) when cultured under normoxic or hypoxic (0.5% O_2) conditions for 20 hours. Scale bars, 50µm. (b) Quantification of the percentage of cells in control or familial RoMS iPSC-pericyte cultures that were EdU^+ after 20 hours of exposure to a normoxic or hypoxic environment. 4-9 wells analysed per line per treatment for n=5 control and n=3 familial RoMS lines. Data are expressed as mean ± SEM, and individual dots represent cell line means. (c,d) Quantification iPSC-pericyte cell area or max feret diameter (max diameter/perimeter) for control and familial RoMS iPSC-pericytes grown under normoxic or hypoxic conditions. > 50 cells measured per cell line per treatment for n=10 control and n=4 familial RoMS lines. Data are expressed as median ± interquartile range, and individual dot points represent cell line means. (e) Images (20X) showing example control iPSC-pericyte morphologies: standard, spindle, sheet and circular. Scale bars, 50 µm. (f) Quantification of the proportion (%) of iPSC pericytes in control or familial RoMS cultures that adopted each morphological subtype when cultured under normoxic or hypoxic conditions. > 22 cells were measured per line per treatment for n=5 control and n=4 familial RoMS lines. Data are expressed as mean ± SEM, individual dot points represent cell line means and was analysed using a binomial generalised linear mixed model. (g) Image (10x) of $Hoechst^+$ control iPSC-pericytes cultured under hypoxic conditions, forming a chain.

Scale bar, 50μm. (h) Quantification of the proportion (%) of iPSC-pericytes forming chains under normoxic and hypoxic conditions. 4-9 wells analysed per line per treatment for n=9 (n=5 control, n=4 familial RoMS) lines. Data for control and familial RoMS lines were combined as the response was equivalent. Data are expressed as median ± interquartile range, and individual dot points represent cell line means. (i) Principal component analysis of gene expression in iPSC-pericytes cultured under normoxic or hypoxic conditions. (j) Volcano plot showing genes that are differentially expressed between iPSC-pericytes cultured under normoxic or hypoxic conditions. Adjusted p-value < 0.05 and Log2 fold change ≥ 0.585; data from n=8 (n=5 control and n=3 familial RoMS) lines were combined as MS status did not impact response to hypoxia. (k) Gene set enrichment indicates the top 6 activated and supressed GO biological process ontology terms associated with hypoxia in iPSC-pericytes. (l) Boxplots showing gene expression in normoxic and hypoxic iPSC pericytes, for differentially expressed genes associated with angiogenesis, cytoskeletal regulation and antigen presentation. Data are expressed as median ± interquartile range, and individual dot points represent cell line means. Restricted maximum likelihood linear mixed model with pairwise comparisons using Tukey's adjustment for p-values. $*p < 0.05$, $**p < 0.01$, $****p < 0.0001$. False discovery rate adjustment was used for multiple testing for RNAseq data.

Figure 6: MS-associated inflammatory cytokines reduce proliferation, increase cell size and enhance contractility. (a) Images (10x) of EdU^+ (red) control iPSC-pericytes following 20 hours of diluent, TNFα, IFNγ or TNFα+IFNγ treatment. Scale bars, 50μm. (b) Quantification of the proportion (%) of cells within control, familial RoMS and sporadic RoMS iPSC-pericyte cultures that incorporated EdU when cultured with diluent, TNFα, IFNγ or TNFα+IFNγ for 20 hours. 4-9 wells were analysed per line per treatment for n=10 control, n=4 familial RoMS and n=8 sporadic RoMS cell lines. Data are expressed as mean ± SEM, and individual dot points represent cell line means. (c) Quantification of control, familial RoMS and sporadic RoMS iPSC-pericyte area for cells cultured with diluent or TNFα+IFNγ. >50 cells were measured per line per treatment for n=10 control and n=4 familial RoMS lines. Data are expressed as median ± interquartile range, and individual dot points represent line mean. (d,e) Normalised xCELLigence cell index of control and familial RoMS iPSC-pericytes cultured with diluent, TNFα, IFNγ or TNFα+IFNγ for 20 hours prior to exposure to ET1. Data are normalised to cell index at the time of endothelin-1 addition. 2-4 wells were analysed per cell line for n=5 control and n=3-4 familial RoMS lines. Data are expressed as mean ± SEM. (f) The fold change in minimum cell index (maximum contraction) after treating control or familial RoMS iPSC-pericytes with diluent, TNFα, IFNγ or TNFα+IFNγ. 2-4 wells were evaluated per cell line for n=5 control and n=3-4 familial RoMS lines. (g) Area under the curve was calculated for the first 50 minutes following iPSC-pericytes exposure to ET-1 for cultures exposed to diluent, TNFα, IFNγ or TNFα+IFNγ. 2-4 wells were evaluated per line for n=5 control and n=3-4 familial RoMS lines. Data are expressed as mean ± SEM. Restricted maximum likelihood linear mixed model with pairwise comparisons using Tukey's adjustment for p-values. $*p < 0.05$, $**p < 0.01$, $***p < 0.001$, $****p < 0.0001$.

References

Absinta, M., Maric, D., Gharagozloo, M., Garton, T., Smith, M.D., Jin, J., Fitzgerald, K.C., Song, A., Liu, P., Lin, J.-P., et al. (2021). A lymphocyte–microglia–astrocyte axis in chronic active multiple sclerosis. Nature *597*, 709-714. 10.1038/s41586-021-03892-7.

Adhya, S., Johnson, G., Herbert, J., Jaggi, H., Babb, J.S., Grossman, R.I., and Inglese, M. (2006). Pattern of hemodynamic impairment in multiple sclerosis: dynamic susceptibility contrast perfusion MR imaging at 3.0 T. Neuroimage *33*, 1029-1035. 10.1016/j.neuroimage.2006.08.008.

Adingupu, D.D., Evans, T., Soroush, A., Hansen, A., Jarvis, S., Brown, L., and Dunn, J.F. (2023). Temporal Pattern of Cortical Hypoxia in Multiple Sclerosis and Its Significance on Neuropsychological and Clinical Measures of Disability. Ann Neurol *94*, 1067-1079. 10.1002/ana.26769.

Alarcon-Martinez, L., Yilmaz-Ozcan, S., Yemisci, M., Schallek, J., Kilic, K., Can, A., Di Polo, A., and Dalkara, T. (2018). Capillary pericytes express alpha-smooth muscle actin, which requires prevention of filamentous-actin depolymerization for detection. Elife *7*. 10.7554/eLife.34861.

Amarasinghe, C., Hossain, M.M., and Jin, J.P. (2016). Functional Basis of Three New Recessive Mutations of Slow Skeletal Muscle Troponin T Found in Non-Amish TNNT1 Nemaline Myopathies. Biochemistry *55*, 4560-4567. 10.1021/acs.biochem.6b00577.

Andueza, A., Kumar, S., Kim, J., Kang, D.W., Mumme, H.L., Perez, J.I., Villa-Roel, N., and Jo, H. (2020). Endothelial Reprogramming by Disturbed Flow Revealed by Single-Cell RNA and Chromatin Accessibility Study. Cell Rep *33*, 108491. 10.1016/j.celrep.2020.108491.

Armulik, A., Genové, G., Mäe, M., Nisancioglu, M.H., Wallgard, E., Niaudet, C., He, L., Norlin, J., Lindblom, P., Strittmatter, K., et al. (2010). Pericytes regulate the blood–brain barrier. Nature *468*, 557-561. 10.1038/nature09522.

Auwera, G.v.d., and O'Connor, B.D. (2020). Genomics in the cloud : using Docker, GATK, and WDL in Terra (O'Reilly Media).

Badia-i-Mompel, P., Santiago, J.V., Braunger, J., Geiss, C., Dimitro, D., Mu¨ller-Dott, S., Taus, P., Dugourd, A., Holland, C.H., Flores, R.O.R., and Saez-Rodriguez, J. (2022). decoupleR: ensemble of computational methods to infer biological activities from omics data. Bioinformatics Advances *2*, 1-3. 10.1093/bioadv/vbac016.

Bankhead, P., Loughrey, M.B., Fernandez, J.A., Dombrowski, Y., McArt, D.G., Dunne, P.D., McQuaid, S., Gray, R.T., Murray, L.J., Coleman, H.G., et al. (2017). QuPath: Open source software for digital pathology image analysis. Sci Rep *7*, 16878. 10.1038/s41598-017-17204-5.

Berthiaume, A.A., Grant, R.I., McDowell, K.P., Underly, R.G., Hartmann, D.A., Levy, M., Bhat, N.R., and Shih, A.Y. (2018). Dynamic Remodeling of Pericytes In Vivo Maintains Capillary Coverage in the Adult Mouse Brain. Cell Rep *22*, 8-16. 10.1016/j.celrep.2017.12.016.

Berthiaume, A.A., Schmid, F., Stamenkovic, S., Coelho-Santos, V., Nielson, C.D., Weber, B., Majesky, M.W., and Shih, A.Y. (2022). Pericyte remodeling is deficient in the aged brain and contributes to impaired capillary flow and structure. Nat Commun *13*, 5912. 10.1038/s41467-022-33464-w.

Blighe, L., Rana, S., and Lewis, M. (2018). EnhancedVolcano: Publication-ready volcano plots with enhanced colouring and labeling.

Brown, L.S., Foster, C.G., Courtney, J.M., King, N.E., Howells, D.W., and Sutherland, B.A. (2019). Pericytes and Neurovascular Function in the Healthy and Diseased Brain. Front Cell Neurosci *13*, 282. 10.3389/fncel.2019.00282.

Brown, L.S., King, N.E., Courtney, J.M., Gasperini, R.J., Foa, L., Howells, D.W., and Sutherland, B.A. (2023). Brain pericytes in culture display diverse morphological and functional phenotypes. Cell Biol Toxicol *39*, 2999-3014. 10.1007/s10565-023-09814-9.

Buch, S., Subramanian, K., Jella, P.K., Chen, Y., Wu, Z., Shah, K., Bernitsas, E., Ge, Y., and Haacke, E.M. (2021). Revealing vascular abnormalities and measuring small vessel density

in multiple sclerosis lesions using USPIO. Neuroimage Clin *29*, 102525. 10.1016/j.nicl.2020.102525.
Burtscher, J., Motl, R.W., Berek, K., Ehrenreich, H., Kopp, M., and Hohenauer, E. (2025). Hypoxia in multiple sclerosis. Redox Biol *83*, 103666. 10.1016/j.redox.2025.103666.
Carlsson, R., Enstrom, A., and Paul, G. (2023). Molecular Regulation of the Response of Brain Pericytes to Hypoxia. Int J Mol Sci *24*. 10.3390/ijms24065671.
Carlsson, R., Ozen, I., Barbariga, M., Gaceb, A., Roth, M., and Paul, G. (2018). STAT3 precedes HIF1alpha transcriptional responses to oxygen and oxygen and glucose deprivation in human brain pericytes. PLoS One *13*, e0194146. 10.1371/journal.pone.0194146.
Cashion, J.M., Brown, L.S., Morris, G.P., Fortune, A.J., Courtney, J.M., Makowiecki, K., Premilovac, D., Cullen, C.L., Young, K.M., and Sutherland, B.A. (2025). Pericyte ablation causes hypoactivity and reactive gliosis in adult mice. Brain Behav Immun. 10.1016/j.bbi.2024.10.014.
Cashion, J.M., Young, K.M., and Sutherland, B.A. (2023). How does neurovascular unit dysfunction contribute to multiple sclerosis? Neurobiol Dis *178*, 106028. 10.1016/j.nbd.2023.106028.
Cembran, A., Eisenbaum, M., Paris, D., Mullan, M., Crawford, F., Ferguson, S., and Bachmeier, C. (2025). Contribution of brain pericytes to neuroinflammation following repetitive head trauma. J Inflamm (Lond) *22*, 11. 10.1186/s12950-025-00439-9.
Coelho-Santos, V., Berthiaume, A.A., Ornelas, S., Stuhlmann, H., and Shih, A.Y. (2021). Imaging the construction of capillary networks in the neonatal mouse brain. Proc Natl Acad Sci U S A *118*. 10.1073/pnas.2100866118.
Cramer, S.P., Simonsen, H., Frederiksen, J.L., Rostrup, E., and Larsson, H.B. (2014). Abnormal blood-brain barrier permeability in normal appearing white matter in multiple sclerosis investigated by MRI. Neuroimage Clin *4*, 182-189. 10.1016/j.nicl.2013.12.001.
D'Haeseleer, M., Beelen, R., Fierens, Y., Cambron, M., Vanbinst, A.M., Verborgh, C., Demey, J., and De Keyser, J. (2013). Cerebral hypoperfusion in multiple sclerosis is reversible and mediated by endothelin-1. Proc Natl Acad Sci U S A *110*, 5654-5658. 10.1073/pnas.1222560110.
de la Pena, M.J., Pena, I.C., Garcia, P.G., Gavilan, M.L., Malpica, N., Rubio, M., Gonzalez, R.A., and de Vega, V.M. (2019). Early perfusion changes in multiple sclerosis patients as assessed by MRI using arterial spin labeling. Acta Radiol Open *8*, 2058460119894214. 10.1177/2058460119894214.
Desai, R.A., Davies, A.L., Del Rossi, N., Tachrount, M., Dyson, A., Gustavson, B., Kaynezhad, P., Mackenzie, L., van der Putten, M.A., McElroy, D., et al. (2020). Nimodipine Reduces Dysfunction and Demyelination in Models of Multiple Sclerosis. Ann Neurol *88*, 123-136. 10.1002/ana.25749.
Dessalles, C.A., Babataheri, A., and Barakat, A.I. (2021). Pericyte mechanics and mechanobiology. J Cell Sci *134*. 10.1242/jcs.240226.
Dias, D.O., Kalkitsas, J., Kelahmetoglu, Y., Estrada, C.P., Tatarishvili, J., Holl, D., Jansson, L., Banitalebi, S., Amiry-Moghaddam, M., Ernst, A., et al. (2021). Pericyte-derived fibrotic scarring is conserved across diverse central nervous system lesions. Nature Communications *12*. 10.1038/s41467-021-25585-5.
Dickson, A.S., Pauzaite, T., Arnaiz, E., Ortmann, B.M., West, J.A., Volkmar, N., Martinelli, A.W., Li, Z., Wit, N., Vitkup, D., et al. (2023). A HIF independent oxygen-sensitive pathway for controlling cholesterol synthesis. Nat Commun *14*, 4816. 10.1038/s41467-023-40541-1.
Downes, N., Niskanen, H., Tomas Bosch, V., Taipale, M., Godiwala, M., Vaananen, M.A., Turunen, T.A., Aavik, E., Laham-Karam, N., Yla-Herttuala, S., and Kaikkonen, M.U. (2023). Hypoxic regulation of hypoxia inducible factor 1 alpha via antisense transcription. J Biol Chem *299*, 105291. 10.1016/j.jbc.2023.105291.
Dyer, E.C., Jacques, A.M., Hoskins, A.C., Ward, D.G., Gallon, C.E., Messer, A.E., Kaski, J.P., Burch, M., Kentish, J.C., and Marston, S.B. (2009). Functional analysis of a unique troponin c mutation, GLY159ASP, that causes familial dilated cardiomyopathy, studied in explanted heart muscle. Circ Heart Fail *2*, 456-464. 10.1161/CIRCHEARTFAILURE.108.818237.

Faal, T., Phan, D.T.T., Davtyan, H., Scarfone, V.M., Varady, E., Blurton-Jones, M., Hughes, C.C.W., and Inlay, M.A. (2019). Induction of Mesoderm and Neural Crest-Derived Pericytes from Human Pluripotent Stem Cells to Study Blood-Brain Barrier Interactions. Stem Cell Reports *12*, 451-460. 10.1016/j.stemcr.2019.01.005.
Faraco, G., Moraga, A., Moore, J., Anrather, J., Pickel, V.M., and Iadecola, C. (2013). Circulating endothelin-1 alters critical mechanisms regulating cerebral microcirculation. Hypertension *62*, 759-766. 10.1161/HYPERTENSIONAHA.113.01761.
Fortune, A.J., Fletcher, J.L., Blackburn, N.B., and Young, K.M. (2022a). Using MS induced pluripotent stem cells to investigate MS aetiology. Multiple Sclerosis and Related Disorders *63*, 103839. 10.1016/j.msard.2022.103839.
Fortune, A.J., Taylor, B.V., Charlesworth, J.C., Burdon, K.P., Blackburn, N.B., Fletcher, J.L., Mehta, A., and Young, K.M. (2022b). Generation and characterisation of four multiple sclerosis iPSC lines from a single family. Stem Cell Res *62*, 102828. 10.1016/j.scr.2022.102828.
Gaitan, M.I., de Alwis, M.P., Sati, P., Nair, G., and Reich, D.S. (2013). Multiple sclerosis shrinks intralesional and enlarges extralesional brain parenchymal veins. Neurology *80*, 145-151. 10.1212/WNL.0b013e31827b916f.
Gharanei, S., Fishwick, K., Peter Durairaj, R., Jin, T., Siamantouras, E., Liu, K.K., Straube, A., Lucas, E.S., Weston, C.J., Rantakari, P., et al. (2020). Vascular Adhesion Protein-1 Determines the Cellular Properties of Endometrial Pericytes. Front Cell Dev Biol *8*, 621016. 10.3389/fcell.2020.621016.
Glahn, D.C., Nimgaonkar, V.L., Raventos, H., Contreras, J., McIntosh, A.M., Thomson, P.A., Jablensky, A., McCarthy, N.S., Charlesworth, J.C., Blackburn, N.B., et al. (2019). Rediscovering the value of families for psychiatric genetics research. Mol Psychiatry *24*, 523-535. 10.1038/s41380-018-0073-x.
Gonul, E., Duz, B., Kahraman, S., Kayali, H., Kubar, A., and Timurkaynak, E. (2002). Early pericyte response to brain hypoxia in cats: an ultrastructural study. Microvasc Res *64*, 116-119. 10.1006/mvre.2002.2413.
Gonzales, A.L., Klug, N.R., Moshkforoush, A., Lee, J.C., Lee, F.K., Shui, B., Tsoukias, N.M., Kotlikoff, M.I., Hill-Eubanks, D., and Nelson, M.T. (2020). Contractile pericytes determine the direction of blood flow at capillary junctions. Proc Natl Acad Sci U S A *117*, 27022-27033. 10.1073/pnas.1922755117.
Guo, X., Xia, S., Ge, T., Lin, Y., Hu, S., Wu, H., Xie, X., Zhang, B., Zhang, S., Zeng, J., et al. (2024). Atp13a5 Marker Reveals Pericyte Specification in the Mouse Central Nervous System. J Neurosci *44*. 10.1523/JNEUROSCI.0727-24.2024.
Halder, S.K., and Milner, R. (2021). Hypoxia in multiple sclerosis; is it the chicken or the egg? Brain *144*, 402-410. 10.1093/brain/awaa427.
Hall, C.N., Reynell, C., Gesslein, B., Hamilton, N.B., Mishra, A., Sutherland, B.A., O'Farrell, F.M., Buchan, A.M., Lauritzen, M., and Attwell, D. (2014). Capillary pericytes regulate cerebral blood flow in health and disease. Nature *508*, 55-60. 10.1038/nature13165.
Hojjat, S.P., Cantrell, C.G., Vitorino, R., Feinstein, A., Shirzadi, Z., MacIntosh, B.J., Crane, D.E., Zhang, L., Morrow, S.A., Lee, L., et al. (2016). Regional reduction in cortical blood flow among cognitively impaired adults with relapsing-remitting multiple sclerosis patients. Mult Scler *22*, 1421-1428. 10.1177/1352458515622696.
Holley, J.E., Newcombe, J., Whatmore, J.L., and Gutowski, N.J. (2010). Increased blood vessel density and endothelial cell proliferation in multiple sclerosis cerebral white matter. Neurosci Lett *470*, 65-70. 10.1016/j.neulet.2009.12.059.
Holtzer, C.A., Marani, E., de Priester, W., and Thomeer, R.T. (1998). The process of decompaction and myelin removal after C7 ventral root avulsion in the cat. Arch Physiol Biochem *106*, 116-127. 10.1076/apab.106.2.116.4389.
Hostenbach, S., D'Haeseleer, M., Kooijman, R., and De Keyser, J. (2019). Modulation of Cytokine-Induced Astrocytic Endothelin-1 Production as a Possible New Approach to the Treatment of Multiple Sclerosis. Front Pharmacol *10*, 1491. 10.3389/fphar.2019.01491.
Huang, D., Cao, L., Xiao, L., Song, J.X., Zhang, Y.J., Zheng, P., and Zheng, S.G. (2019). Hypoxia induces actin cytoskeleton remodeling by regulating the binding of CAPZA1 to F-actin

via PIP2 to drive EMT in hepatocellular carcinoma. Cancer Lett *448*, 117-127. 10.1016/j.canlet.2019.01.042.
Hung, C.F., Holton, S., Chow, Y.H., Liles, W.C., Gharib, S.A., and Altemeier, W.A. (2021). Pericyte-like cells undergo transcriptional reprogramming and distinct functional adaptations in acute lung injury. FASEB J *35*, e21323. 10.1096/fj.201903192RR.
International Multiple Sclerosis Genetics Consortium (2019). Multiple sclerosis genomic map implicates peripheral immune cells and microglia in susceptibility. Science *365*, eaav7188. 10.1126/science.aav7188.
Islam, M.M., Gaska, I., Oshinowo, O., Otumala, A., Shekhar, S., Au Yong, N., and Myers, D.R. (2024). Single-pericyte nanomechanics measured by contraction cytometry. APL Bioeng *8*, 036109. 10.1063/5.0213761.
Jäkel, S., Agirre, E., Mendanha Falcão, A., Van Bruggen, D., Lee, K.W., Knuesel, I., Malhotra, D., Ffrench-Constant, C., Williams, A., and Castelo-Branco, G. (2019). Altered human oligodendrocyte heterogeneity in multiple sclerosis. Nature *566*, 543-547. 10.1038/s41586-019-0903-2.
Jakimovski, D., Gibney, B.L., Marr, K., Ramasamy, D.P., Dwyer, M.G., Bergsland, N., Weinstock-Guttman, B., Ramanathan, M., and Zivadinov, R. (2022). Lower cerebral arterial blood flow is associated with greater serum neurofilament light chain levels in multiple sclerosis patients. Eur J Neurol *29*, 2299-2308. 10.1111/ene.15374.
Jakimovski, D., Qureshi, F., Ramanathan, M., Keshavan, A., Leyden, K., Jalaleddini, K., Ghoreyshi, A., Dwyer, M.G., Bergsland, N., Marr, K., et al. (2024). Lower arterial cerebral blood flow is associated with worse neuroinflammation and immunomodulation composite proteomic scores. Mult Scler Relat Disord *87*, 105687. 10.1016/j.msard.2024.105687.
Javerzat, S., Franco, M., Herbert, J., Platonova, N., Peille, A.-L., Pantesco, V., De Vos, J., Assou, S., Bicknell, R., Bikfalvi, A., and Hagedorn, M. (2009). Correlating Global Gene Regulation to Angiogenesis in the Developing Chick Extra-Embryonic Vascular System. PLoS ONE *4*, e7856. 10.1371/journal.pone.0007856.
Johnston, J.R., Chase, B., and Pinto, J.R. (2018). Troponin through the looking-glass: emerging roles beyond regulation of striated muscle contraction. Oncotarget *9*, 1461-1482. 10.18632/oncotarget.22879.
Jokubaitis, V.G., Campagna, M.P., Ibrahim, O., Stankovich, J., Kleinova, P., Matesanz, F., Hui, D., Eichau, S., Slee, M., Lechner-Scott, J., et al. (2023). Not all roads lead to the immune system: the genetic basis of multiple sclerosis severity. Brain *146*, 2316-2331. 10.1093/brain/awac449.
Karczewski, K.J., Francioli, L.C., Tiao, G., Cummings, B.B., Alföldi, J., Wang, Q., Collins, R.L., Laricchia, K.M., Ganna, A., Birnbaum, D.P., et al. (2020). The mutational constraint spectrum quantified from variation in 141,456 humans. Nature *581*, 434-443. 10.1038/s41586-020-2308-7.
Kaushik, D.K., Bhattacharya, A., Lozinski, B.M., and Wee Yong, V. (2021). Pericytes as mediators of infiltration of macrophages in multiple sclerosis. J Neuroinflammation *18*, 301. 10.1186/s12974-021-02358-x.
King, N.E., Courtney, J.M., Brown, L.S., Fortune, A.J., Blackburn, N.B., Fletcher, J.L., Cashion, J.M., Talbot, J., Pebay, A., Hewitt, A.W., et al. (2024). Induced pluripotent stem cell derived pericytes respond to mediators of proliferation and contractility. Stem Cell Res Ther *15*, 59. 10.1186/s13287-024-03671-x.
King, N.E., Courtney, J.M., Brown, L.S., Foster, C.G., Cashion, J.M., Attrill, E., Premilovac, D., Howells, D.W., and Sutherland, B.A. (2022). Pharmacological PDGFRbeta inhibitors imatinib and sunitinib cause human brain pericyte death in vitro. Toxicol Appl Pharmacol *444*, 116025. 10.1016/j.taap.2022.116025.
Kolde, R. (2012). Pheatmap: pretty heatmaps.
Korte, N., Barkaway, A., Wells, J., Freitas, F., Sethi, H., Andrews, S.P., Skidmore, J., Stevens, B., and Attwell, D. (2024). Inhibiting Ca(2+) channels in Alzheimer's disease model mice relaxes pericytes, improves cerebral blood flow and reduces immune cell stalling and hypoxia. Nat Neurosci *27*, 2086-2100. 10.1038/s41593-024-01753-w.

Krueger, F., James, F., Ewels, P., Afyounian, E., Weinstein, M., Schuster-Boeckler, B., Hulselmans, G., and sclamons (2023). TrimGalore: v0.6.10. Zenodo. 10.5281/zenodo.7598955.
Kutcher, M.E., Kolyada, A.Y., Surks, H.K., and Herman, I.M. (2007). Pericyte Rho GTPase mediates both pericyte contractile phenotype and capillary endothelial growth state. Am J Pathol *171*, 693-701. 10.2353/ajpath.2007.070102.
Law, M., Saindane, A.M., Ge, Y., Babb, J.S., Johnson, G., Mannon, L.J., Herbert, J., and Grossman, R.I. (2004). Microvascular Abnormality in Relapsing-Remitting Multiple Sclerosis: Perfusion MR Imaging Findings in Normal-appearing White Matter. Radiology *231*. 10.1148/radiol.2313030996.
Leech, S., Kirk, J., Plumb, J., and McQuaid, S. (2007). Persistent endothelial abnormalities and blood-brain barrier leak in primary and secondary progressive multiple sclerosis. Neuropathol Appl Neurobiol *33*, 86-98. 10.1111/j.1365-2990.2006.00781.x.
Li, H., He, Y., Wang, Y., Xie, L., Wu, G., Liu, X., Duan, X., Zhou, K., and Ning, W. (2024a). The RhoGAP ARHGAP32 interacts with desmoplakin, and is required for desmosomal organization and assembly. J Cell Sci *137*. 10.1242/jcs.261901.
Li, X., Xiang, C., Zhu, S., Guo, J., Liu, C., Wang, A., Cao, J., Lu, Y., Neculai, D., Xu, P., and Feng, X.H. (2024b). SNX8 enables lysosome reformation and reverses lysosomal storage disorder. Nat Commun *15*, 2553. 10.1038/s41467-024-46705-x.
Liu, M., Zhao, P., Feng, H., Yang, Y., Zhang, X., Chen, E., Xiao, H., Luo, J., Chen, H., Yin, J., et al. (2025). Biglycan stimulates retinal pathological angiogenesis via up-regulation of CXCL12 expression in pericytes. FASEB J *39*, e70262. 10.1096/fj.202401903R.
Love, M.I., Huber, W., and Anders, S. (2014). Moderated estimation of fold change and dispersion for RNA-seq data with DESeq2. Genome Biology *15*. 10.1186/s13059-014-0550-8.
Ma, Q., Zhao, Z., Sagare, A.P., Wu, Y., Wang, M., Owens, N.C., Verghese, P.B., Herz, J., Holtzman, D.M., and Zlokovic, B.V. (2018). Blood-brain barrier-associated pericytes internalize and clear aggregated amyloid-beta42 by LRP1-dependent apolipoprotein E isoform-specific mechanism. Mol Neurodegener *13*, 57. 10.1186/s13024-018-0286-0.
Macharia, L.W., Muriithi, W., Heming, C.P., Nyaga, D.K., Aran, V., Mureithi, M.W., Ferrer, V.P., Pane, A., Filho, P.N., and Moura-Neto, V. (2021). The genotypic and phenotypic impact of hypoxia microenvironment on glioblastoma cell lines. BMC Cancer *21*, 1248. 10.1186/s12885-021-08978-z.
Macnair, W., Calini, D., Agirre, E., Bryois, J., Jakel, S., Smith, R.S., Kukanja, P., Stokar-Regenscheit, N., Ott, V., Foo, L.C., et al. (2025). snRNA-seq stratifies multiple sclerosis patients into distinct white matter glial responses. Neuron *113*, 396-410 e399. 10.1016/j.neuron.2024.11.016.
Marshall, O., Chawla, S., Lu, H., Pape, L., and Ge, Y. (2016). Cerebral blood flow modulation insufficiency in brain networks in multiple sclerosis: A hypercapnia MRI study. J Cereb Blood Flow Metab *36*, 2087-2095. 10.1177/0271678X16654922.
Marshall, O., Lu, H., Brisset, J.C., Xu, F., Liu, P., Herbert, J., Grossman, R.I., and Ge, Y. (2014). Impaired cerebrovascular reactivity in multiple sclerosis. JAMA Neurol *71*, 1275-1281. 10.1001/jamaneurol.2014.1668.
Mascali, D., Villani, A., Chiarelli, A.M., Biondetti, E., Lipp, I., Digiovanni, A., Pozzilli, V., Caporale, A.S., Rispoli, M.G., Ajdinaj, P., et al. (2023). Pathophysiology of multiple sclerosis damage and repair: Linking cerebral hypoperfusion to the development of irreversible tissue loss in multiple sclerosis using magnetic resonance imaging. Eur J Neurol *30*, 2348-2356. 10.1111/ene.15827.
McLaren, W., Gil, L., Hunt, S.E., Riat, H.S., Ritchie, G.R., Thormann, A., Flicek, P., and Cunningham, F. (2016). The Ensembl Variant Effect Predictor. Genome Biol *17*, 122. 10.1186/s13059-016-0974-4.
Mehta, A., Lu, P., Taylor, B.V., Charlesworth, J., Cook, A., Burdon, K., Hewitt, A., and Young, K.M. (2021). Generation of MNZTASi001-A, a human pluripotent stem cell line from a person

with primary progressive multiple sclerosis. Stem Cell Research *57*, 102568. 10.1016/j.scr.2021.102568.
Mujanovic, A., Ng, F., Meinel, T.R., Dobrocky, T., Piechowiak, E.I., Kurmann, C.C., Seiffge, D.J., Wegener, S., Wiest, R., Meyer, L., et al. (2024). No-reflow phenomenon in stroke patients: A systematic literature review and meta-analysis of clinical data. Int J Stroke *19*, 58-67. 10.1177/17474930231180434.
Neuhaus, A.A., Couch, Y., Sutherland, B.A., and Buchan, A.M. (2017). Novel method to study pericyte contractility and responses to ischaemia in vitro using electrical impedance. J Cereb Blood Flow Metab *37*, 2013-2024. 10.1177/0271678X16659495.
Nikolakopoulou, A.M., Montagne, A., Kisler, K., Dai, Z., Wang, Y., Huuskonen, M.T., Sagare, A.P., Lazic, D., Sweeney, M.D., Kong, P., et al. (2019). Pericyte loss leads to circulatory failure and pleiotrophin depletion causing neuron loss. Nat Neurosci *22*, 1089-1098. 10.1038/s41593-019-0434-z.
Nishihara, H., Perriot, S., Gastfriend, B.D., Steinfort, M., Cibien, C., Soldati, S., Matsuo, K., Guimbal, S., Mathias, A., Palecek, S.P., et al. (2022). Intrinsic blood–brain barrier dysfunction contributes to multiple sclerosis pathogenesis. Brain *145*, 4334-4348. 10.1093/brain/awac019.
Papadaki, E.Z., Mastorodemos, V.C., Amanakis, E.Z., Tsekouras, K.C., Papadakis, A.E., Tsavalas, N.D., Simos, P.G., Karantanas, A.H., Plaitakis, A., and Maris, T.G. (2012). White matter and deep gray matter hemodynamic changes in multiple sclerosis patients with clinically isolated syndrome. Magn Reson Med *68*, 1932-1942. 10.1002/mrm.24194.
Patel, H., Ewels, P., Peltzer, A., Botvinnik, O., Sturm, G., Moreno, D., Vemuri, P., Garcia, M.U., silviamorins, Pantano, L., et al. (2023). nf-core/rnaseq: nf-core/rnaseq v3.12.0 - Osmium Octopus (3.12.0). Zenodo. 10.5281/zenodo.7998767.
Pedersen, B.S., Bhetariya, P.J., Brown, J., Kravitz, S.N., Marth, G., Jensen, R.L., Bronner, M.P., Underhill, H.R., and Quinlan, A.R. (2020). Somalier: rapid relatedness estimation for cancer and germline studies using efficient genome sketches. Genome Med *12*, 62. 10.1186/s13073-020-00761-2.
Pedersen, B.S., and Quinlan, A.R. (2018). Mosdepth: quick coverage calculation for genomes and exomes. Bioinformatics *34*, 867-868. 10.1093/bioinformatics/btx699.
Plumb, J., Mcquaid, S., Mirakhur, M., and Kirk, J. (2002). Abnormal Endothelial Tight Junctions in Active Lesions and Normal-appearing White Matter in Multiple Sclerosis. Brain Pathology *12*, 154-169. 10.1111/j.1750-3639.2002.tb00430.x.
Ponath, G., Ramanan, S., Mubarak, M., Housley, W., Lee, S., Sahinkaya, F.R., Vortmeyer, A., Raine, C.S., and Pitt, D. (2017). Myelin phagocytosis by astrocytes after myelin damage promotes lesion pathology. Brain *140*, 399-413. 10.1093/brain/aww298.
Poplin, R., Ruano-Rubio, V., DePristo, M.A., Fennell, T.J., Carneiro, M.O., Van der Auwera, G.A., Kling, D.E., Gauthier, L.D., Levy-Moonshine, A., Roazen, D., et al. (2018). Scaling accurate genetic variant discovery to tens of thousands of samples. Biorxiv. 10.1101/201178.
Provenzano, P.P., and Keely, P.J. (2011). Mechanical signaling through the cytoskeleton regulates cell proliferation by coordinated focal adhesion and Rho GTPase signaling. J Cell Sci *124*, 1195-1205. 10.1242/jcs.067009.
Ren, S.Y., Xia, Y., Yu, B., Lei, Q.J., Hou, P.F., Guo, S., Wu, S.L., Liu, W., Yang, S.F., Jiang, Y.B., et al. (2024). Growth hormone promotes myelin repair after chronic hypoxia via triggering pericyte-dependent angiogenesis. Neuron *112*, 2177-2196 e2176. 10.1016/j.neuron.2024.03.026.
Ribatti, D., Nico, B., and Crivellato, E. (2011). The role of pericytes in angiogenesis. Int J Dev Biol *55*, 261-268. 10.1387/ijdb.103167dr.
Risso, D., Ngai, J., Speed, T.P., and Dudoit, S. (2014). Normalization of RNA-seq data using factor analysis of control genes or samples. Nature Biotechnology *32*, 896-902. 10.1038/nbt.2931.
Rolfe, A.J., Bosco, D.B., Broussard, E.N., and Ren, Y. (2017). In Vitro Phagocytosis of Myelin Debris by Bone Marrow-Derived Macrophages. J Vis Exp. 10.3791/56322.
Schmoranzer, J., Fawcett, J.P., Segura, M., Tan, S., Vallee, R.B., Pawson, T., and Gundersen, G.G. (2009). Par3 and Dynein Associate to Regulate Local Microtubule Dynamics

and Centrosome Orientation during Migration. Current Biology *19*, 1065-1074. 10.1016/j.cub.2009.05.065.
Schubach, M., Maass, T., Nazaretyan, L., Roner, S., and Kircher, M. (2024). CADD v1.7: using protein language models, regulatory CNNs and other nucleotide-level scores to improve genome-wide variant predictions. Nucleic Acids Res *52*, D1143-D1154. 10.1093/nar/gkad989.
Singh, T., Poterba, T., Curtis, D., Akil, H., Al Eissa, M., Barchas, J.D., Bass, N., Bigdeli, T.B., Breen, G., Bromet, E.J., et al. (2022). Rare coding variants in ten genes confer substantial risk for schizophrenia. Nature *604*, 509-516. 10.1038/s41586-022-04556-w.
Sisco, N.J., Borazanci, A., Dortch, R., and Stokes, A.M. (2021). Investigating the relationship between multi-scale perfusion and white matter microstructural integrity in patients with relapsing-remitting MS. Mult Scler J Exp Transl Clin *7*, 20552173211037002. 10.1177/20552173211037002.
Sodhi, A., Ma, T., Menon, D., Deshpande, M., Jee, K., Dinabandhu, A., Vancel, J., Lu, D., and Montaner, S. (2019). Angiopoietin-like 4 binds neuropilins and cooperates with VEGF to induce diabetic macular edema. J Clin Invest *129*, 4593-4608. 10.1172/JCI120879.
Soneson, C., Love, M.I., and Robinson, M.D. (2015). Differential analyses for RNA-seq: transcript-level estimates improve gene-level inferences. F1000Research *4*, 1521. 10.12688/f1000research.7563.1.
Stickland, R., Allen, M., Magazzini, L., Singh, K.D., Wise, R.G., and Tomassini, V. (2019). Neurovascular Coupling During Visual Stimulation in Multiple Sclerosis: A MEG-fMRI Study. Neuroscience *403*, 54-69. 10.1016/j.neuroscience.2018.03.018.
Thievessen, I., Suhr, F., Vergarajauregui, S., Bottcher, R.T., Brixius, K., Rosenberger, G., Dewald, O., Fleischmann, B.K., Ghanem, A., Kruger, M., et al. (2022). The focal adhesion protein beta-parvin controls cardiomyocyte shape and sarcomere assembly in response to mechanical load. Curr Biol *32*, 3033-3047 e3039. 10.1016/j.cub.2022.05.047.
Tigges, U., Boroujerdi, A., Welser-Alves, J.V., and Milner, R. (2013). TNF-a promotes cerebral pericyte remodeling in vitro, via a switch from a1 to a2 integrins. Journal of Neuroinflammation *10*. 10.1186/1742-2094-10-33.
Torok, O., Schreiner, B., Schaffenrath, J., Tsai, H.C., Maheshwari, U., Stifter, S.A., Welsh, C., Amorim, A., Sridhar, S., Utz, S.G., et al. (2021). Pericytes regulate vascular immune homeostasis in the CNS. Proc Natl Acad Sci U S A *118*. 10.1073/pnas.2016587118.
Varga, A.W., Johnson, G., Babb, J.S., Herbert, J., Grossman, R.I., and Inglese, M. (2009). White matter hemodynamic abnormalities precede sub-cortical gray matter changes in multiple sclerosis. J Neurol Sci *282*, 28-33. 10.1016/j.jns.2008.12.036.
Wang, K., Li, M., and Hakonarson, H. (2010). ANNOVAR: functional annotation of genetic variants from high-throughput sequencing data. Nucleic Acids Res *38*, e164. 10.1093/nar/gkq603.
Williams, T., Lange, F., Smith, K.J., Tachtsidis, I., and Chataway, J. (2024). Investigating cortical hypoxia in multiple sclerosis via time-domain near-infrared spectroscopy. Ann Clin Transl Neurol *11*, 2372-2381. 10.1002/acn3.52150.
Woo, M.S., Engler, J.B., and Friese, M.A. (2024). The neuropathobiology of multiple sclerosis. Nat Rev Neurosci *25*, 493-513. 10.1038/s41583-024-00823-z.
Wu, T., Hu, E., Xu, S., Chen, M., Guo, P., Dai, Z., Feng, T., Zhou, L., Tang, W., Zhan, L., et al. (2021). clusterProfiler 4.0: A universal enrichment tool for interpreting omics data. The Innovation *2*, 100141. 10.1016/j.xinn.2021.100141.
Yang, R., and Dunn, J.F. (2015). Reduced cortical microvascular oxygenation in multiple sclerosis: a blinded, case-controlled study using a novel quantitative near-infrared spectroscopy method. Sci Rep *5*, 16477. 10.1038/srep16477.
Yemisci, M., Gursoy-Ozdemir, Y., Vural, A., Can, A., Topalkara, K., and Dalkara, T. (2009). Pericyte contraction induced by oxidative-nitrative stress impairs capillary reflow despite successful opening of an occluded cerebral artery. Nat Med *15*, 1031-1037. 10.1038/nm.2022.
Zhang, Y., Chen, K., Sloan, S.A., Bennett, M.L., Scholze, A.R., O'Keeffe, S., Phatnani, H.P., Guarnieri, P., Caneda, C., Ruderisch, N., et al. (2014). An RNA-sequencing transcriptome and

splicing database of glia, neurons, and vascular cells of the cerebral cortex. J Neurosci *34*, 11929-11947. 10.1523/JNEUROSCI.1860-14.2014.
Zhou, T., Zheng, Y., Sun, L., Badea, S.R., Jin, Y., Liu, Y., Rolfe, A.J., Sun, H., Wang, X., Cheng, Z., et al. (2019a). Microvascular endothelial cells engulf myelin debris and promote macrophage recruitment and fibrosis after neural injury. Nat Neurosci *22*, 421-435. 10.1038/s41593-018-0324-9.
Zhou, Y., Zhou, B., Pache, L., Chang, M., Khodabakhshi, A.H., Tanaseichuk, O., Benner, C., and Chanda, S.K. (2019b). Metascape provides a biologist-oriented resource for the analysis of systems-level datasets. Nat Commun *10*, 1523. 10.1038/s41467-019-09234-6.
Zierfuss, B., Larochelle, C., and Prat, A. (2024). Blood-brain barrier dysfunction in multiple sclerosis: causes, consequences, and potential effects of therapies. Lancet Neurol *23*, 95-109. 10.1016/S1474-4422(23)00377-0.

hPSC[reg®] Line	Group	Sex	Age at Collection
MNZTASi009-A	Control	F	[redacted]
MNZTASi019-A	Control	F	
MNZTASi020-A	Control	F	
MNZTASi021-A	Control	M	
MNZTASi022-A	Control	F	
MNZTASi024-A	Control	F	
MNZTASi032-A	Control	M	
MNZTASi040-A	Control	M	
MNZTASi050-A	Control	M	
MNZTASi070-A	Control	M	
MNZTASi002-A	Familial RoMS	F	
MNZTASi003-A	Familial RoMS	F	
MNZTASi004-A	Familial RoMS	F	
MNZTASi005-A	Familial RoMS	M	
MNZTASi007-A	Sporadic RoMS	F	
MNZTASi010-A	Sporadic RoMS	F	
MNZTASi014-A	Sporadic RoMS	F	
MNZTASi016-A	Sporadic RoMS	F	
MNZTASi017-A	Sporadic RoMS	F	
MNZTASi018-A	Sporadic RoMS	F	
MNZTASi033-A	Sporadic RoMS	M	
MNZTASi037-A	Sporadic RoMS	M	

Table 1: iPSC line details and disease status

Figures

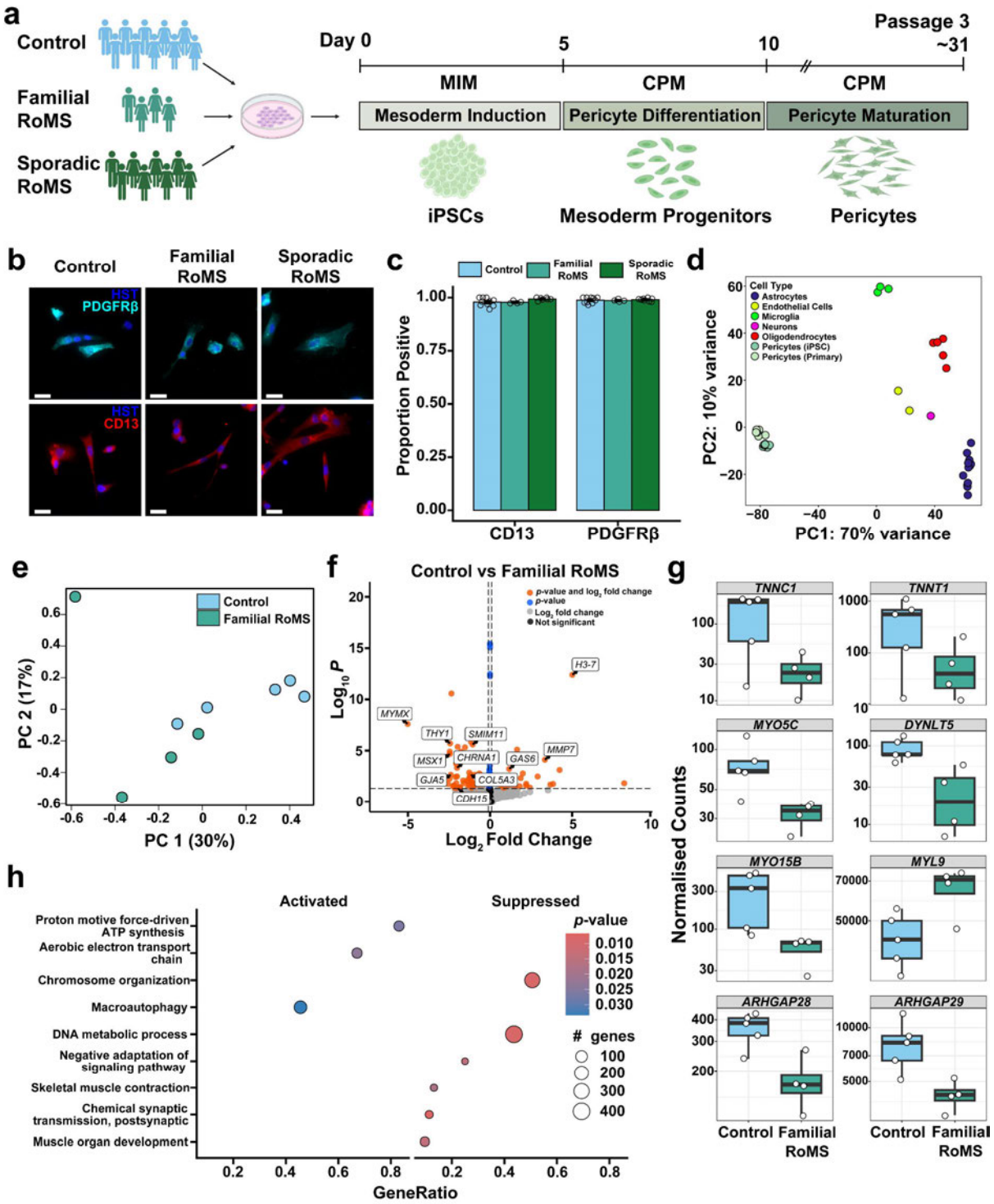

Figure 1

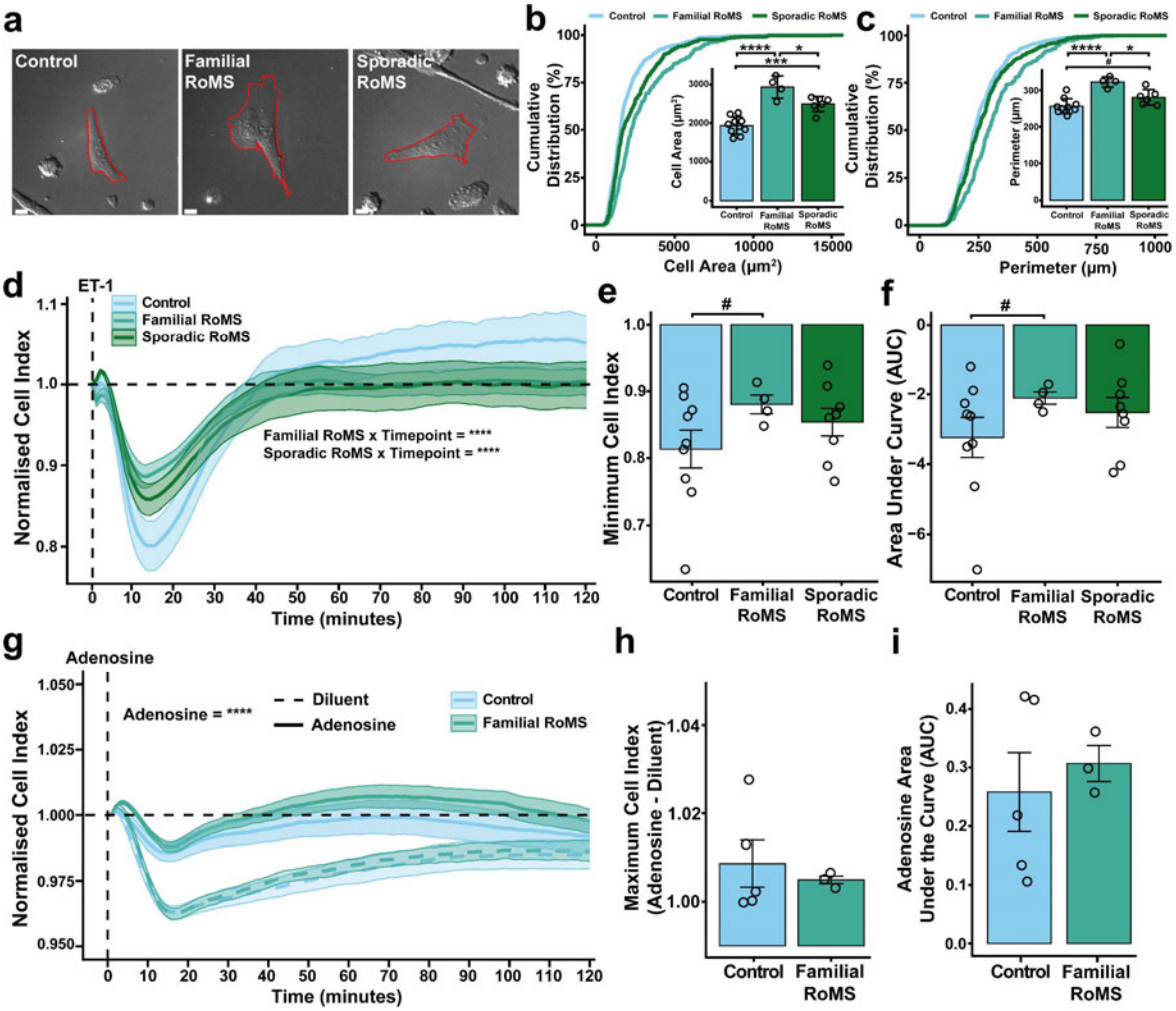
a
Control
Familial RoMS
Sporadic RoMS
b
Control
Familial RoMS
Sporadic RoMS
Cumulative Distribution (%)
Cell Area (µm²)
Cell Area (µm²)
c
Perimeter (µm)
d
ET-1
Normalised Cell Index
Time (minutes)
Familial RoMS x Timepoint = ****
Sporadic RoMS x Timepoint = ****
e
Minimum Cell Index
f
Area Under Curve (AUC)
g
Adenosine
Adenosine = ****
Diluent
Adenosine
h
Maximum Cell Index (Adenosine - Diluent)
i
Adenosine Area Under the Curve (AUC)

Figure 2

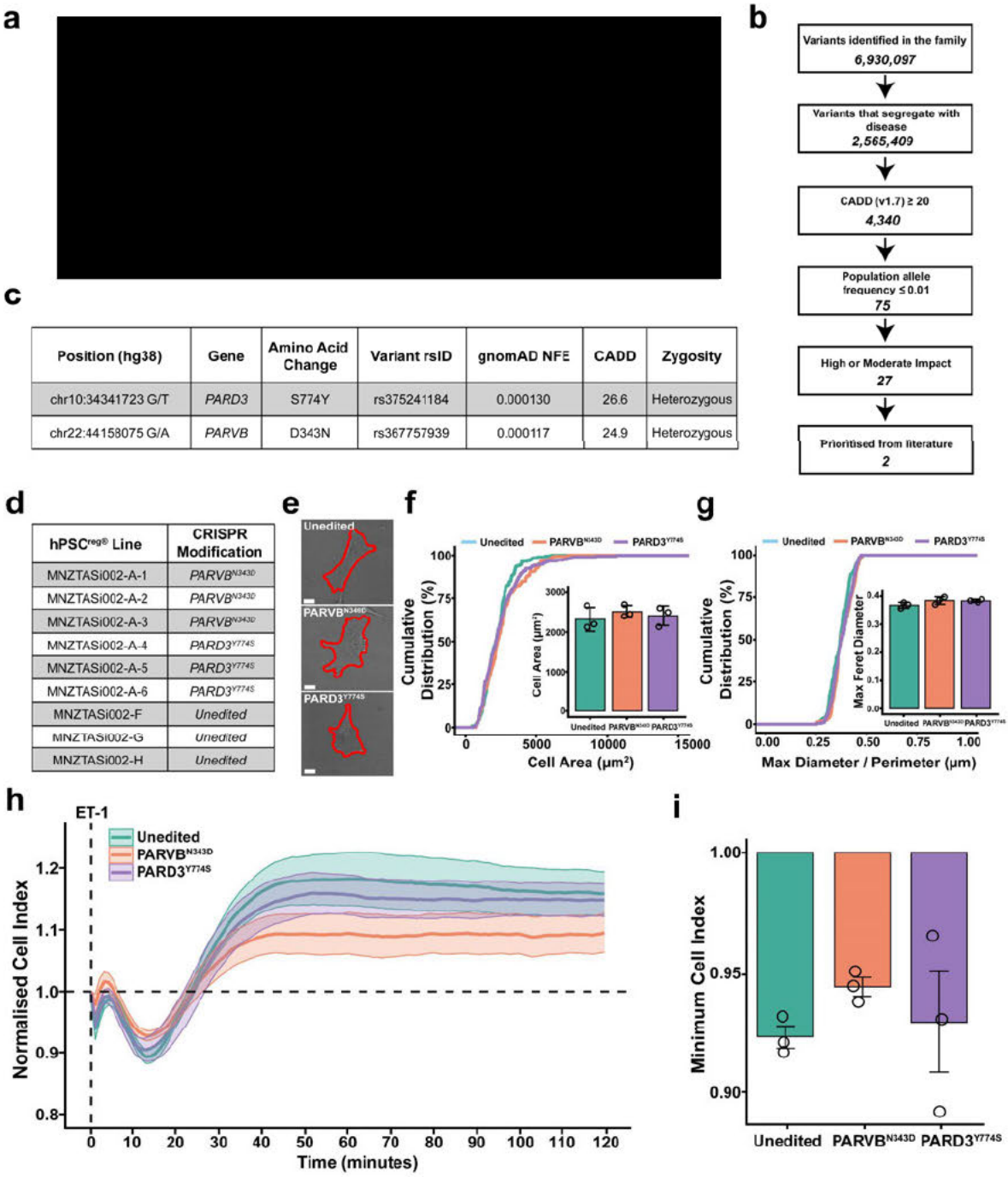

Position (hg38)	Gene	Amino Acid Change	Variant rsID	gnomAD NFE	CADD	Zygosity
chr10:34341723 G/T	*PARD3*	S774Y	rs375241184	0.000130	26.6	Heterozygous
chr22:44158075 G/A	*PARVB*	D343N	rs367757939	0.000117	24.9	Heterozygous

hPSC$^{reg®}$ Line	CRISPR Modification
MNZTASi002-A-1	*PARVB*^{N343D}
MNZTASi002-A-2	*PARVB*^{N343D}
MNZTASi002-A-3	*PARVB*^{N343D}
MNZTASi002-A-4	*PARD3*^{Y774S}
MNZTASi002-A-5	*PARD3*^{Y774S}
MNZTASi002-A-6	*PARD3*^{Y774S}
MNZTASi002-F	*Unedited*
MNZTASi002-G	*Unedited*
MNZTASi002-H	*Unedited*

Figure 3

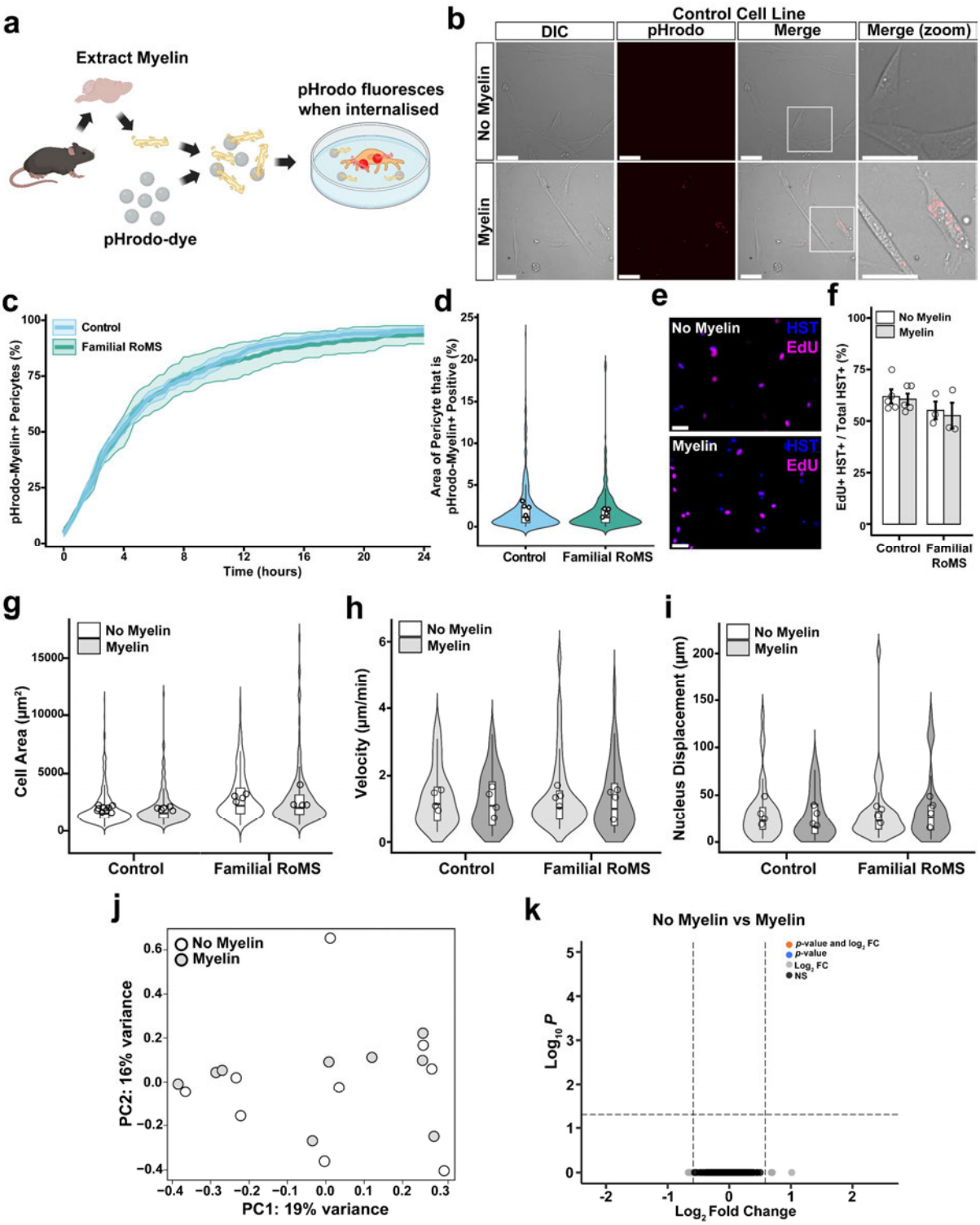
a
Extract Myelin
pHrodo fluoresces when internalised
pHrodo-dye
b
Control Cell Line
DIC
pHrodo
Merge
Merge (zoom)
No Myelin
Myelin
c
Control
Familial RoMS
pHrodo-Myelin+ Pericytes (%)
Time (hours)
d
Area of Pericyte that is pHrodo-Myelin+ Positive (%)
Control
Familial RoMS
e
No Myelin
Myelin
HST
EdU
f
No Myelin
Myelin
EdU+ HST+ / Total HST+ (%)
Control
Familial RoMS
g
No Myelin
Myelin
Cell Area (µm²)
Control
Familial RoMS
h
No Myelin
Myelin
Velocity (µm/min)
Control
Familial RoMS
i
No Myelin
Myelin
Nucleus Displacement (µm)
Control
Familial RoMS
j
No Myelin
Myelin
PC2: 16% variance
PC1: 19% variance
k
No Myelin vs Myelin
p-value and log2 FC
p-value
Log2 FC
NS
Log10 P
Log2 Fold Change

Figure 4

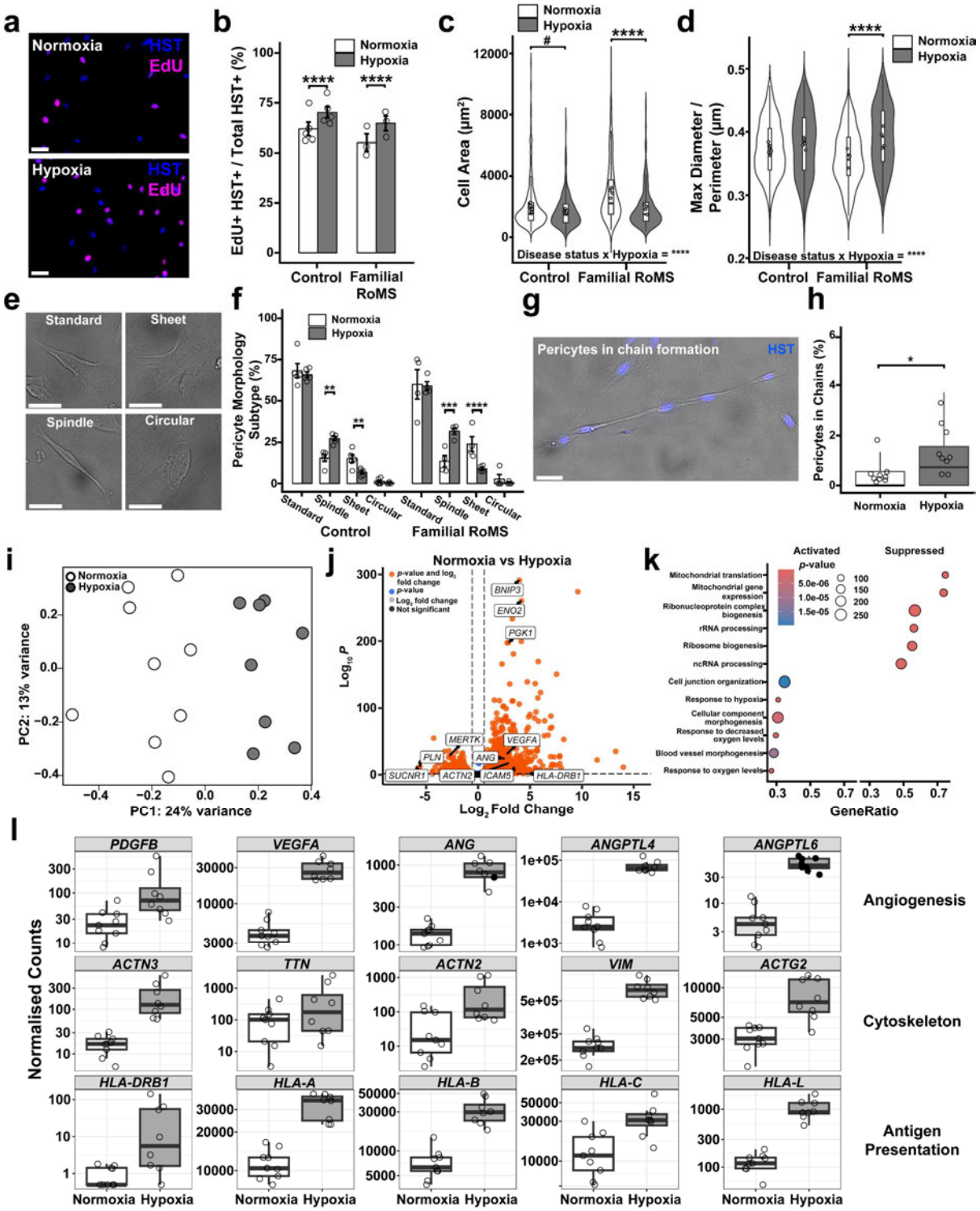
a
Normoxia
HST
EdU
Hypoxia
HST
EdU
b
Normoxia
Hypoxia
EdU+ HST+ / Total HST+ (%)
****
****
Control
Familial RoMS
c
Normoxia
Hypoxia
Cell Area (µm²)
#
****
Disease status x Hypoxia = ****
Control
Familial RoMS
d
Normoxia
Hypoxia
Max Diameter / Perimeter (µm)
****
Disease status x Hypoxia = ****
Control
Familial RoMS
e
Standard
Sheet
Spindle
Circular
f
Normoxia
Hypoxia
Pericyte Morphology Subtype (%)
Standard
Spindle
Sheet
Circular
Control
Familial RoMS
g
Pericytes in chain formation
HST
h
Pericytes in Chains (%)
Normoxia
Hypoxia
i
Normoxia
Hypoxia
PC2: 13% variance
PC1: 24% variance
j
Normoxia vs Hypoxia
p-value and log2 fold change
p-value
Log2 fold change
Not significant
BNIP3
ENO2
PGK1
MERTK
VEGFA
PLN
ANG
SUCNR1
ACTN2
ICAM5
HLA-DRB1
Log10 P
Log2 Fold Change
k
Activated
Suppressed
p-value
5.0e-06
1.0e-05
1.5e-05
Mitochondrial translation
Mitochondrial gene expression
Ribonucleoprotein complex biogenesis
rRNA processing
Ribosome biogenesis
ncRNA processing
Cell junction organization
Response to hypoxia
Cellular component morphogenesis
Response to decreased oxygen levels
Blood vessel morphogenesis
Response to oxygen levels
GeneRatio
l
Normalised Counts
PDGFB
VEGFA
ANG
ANGPTL4
ANGPTL6
Angiogenesis
ACTN3
TTN
ACTN2
VIM
ACTG2
Cytoskeleton
HLA-DRB1
HLA-A
HLA-B
HLA-C
HLA-L
Antigen Presentation
Normoxia
Hypoxia

Figure 5

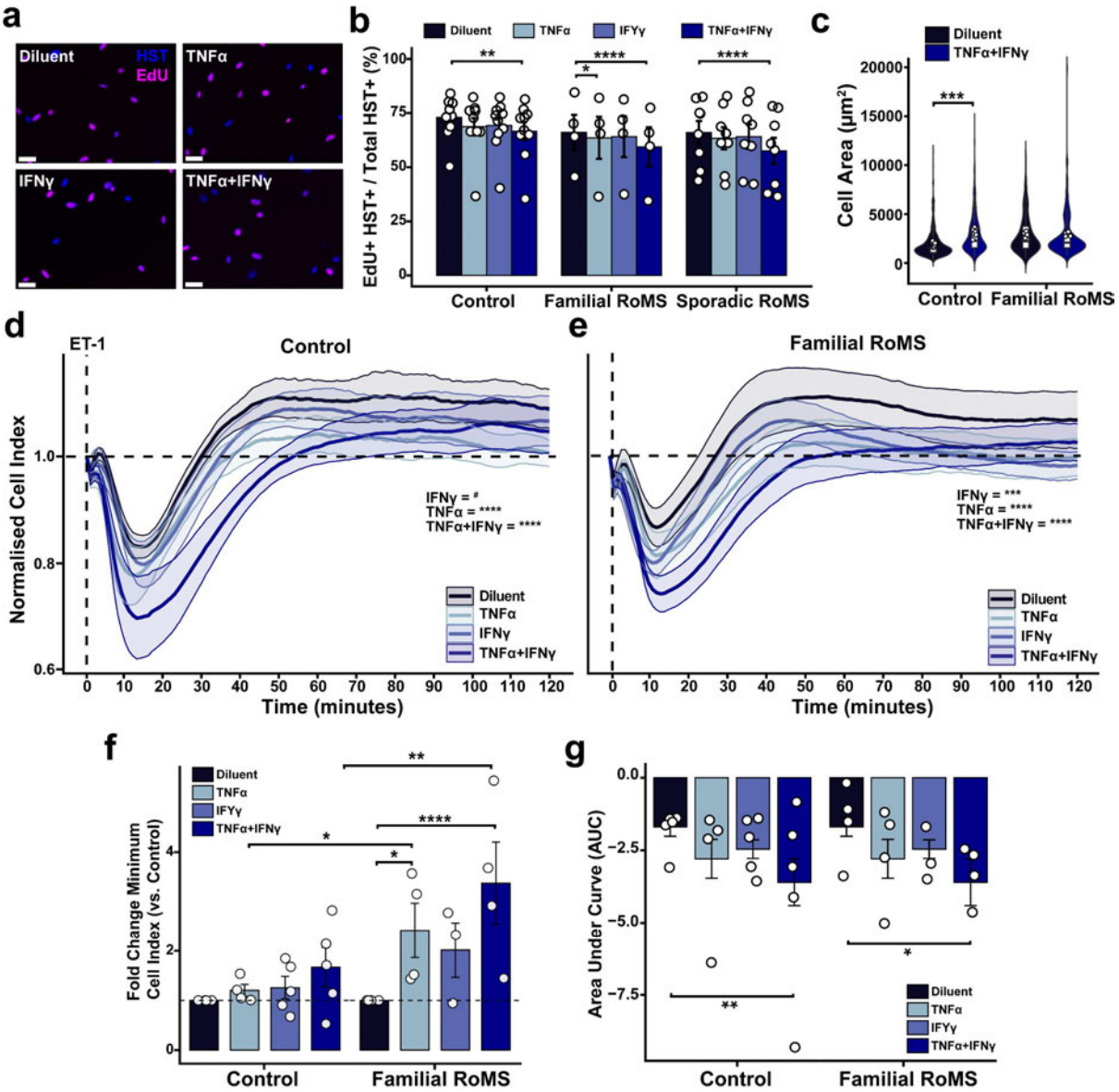
a
Diluent
HST
EdU
TNFα
IFNγ
TNFα+IFNγ
b
Diluent
TNFα
IFYγ
TNFα+IFNγ
EdU+ HST+ / Total HST+ (%)
Control
Familial RoMS
Sporadic RoMS
c
Diluent
TNFα+IFNγ
Cell Area (μm²)
Control
Familial RoMS
d
ET-1
Control
Normalised Cell Index
IFNγ = #
TNFα = ****
TNFα+IFNγ = ****
Diluent
TNFα
IFNγ
TNFα+IFNγ
Time (minutes)
e
Familial RoMS
IFNγ = ***
TNFα = ****
TNFα+IFNγ = ****
Diluent
TNFα
IFNγ
TNFα+IFNγ
Time (minutes)
f
Diluent
TNFα
IFYγ
TNFα+IFNγ
Fold Change Minimum Cell Index (vs. Control)
Control
Familial RoMS
g
Area Under Curve (AUC)
Diluent
TNFα
IFYγ
TNFα+IFNγ
Control
Familial RoMS

Figure 6